Targeting Lysosomal pH Restores Mitochondrial Quality Control in GBA1-Mutant Parkinson's Disease

Preethi Sheshadri[1,†,*],
Maria Alicia Costa Besada[1,#],
Alessia Fisher[1],
Szilvia Kiraly[2],
Kritarth Singh[1],
Ioanna Kourouzidou[1,‡],
Thomas S. Blacker[3]
Jialiu Zeng[4,§]
Orian S Shirihai[5],
Mark W Grinstaff[4],
Michael R Duchen[1,*].

1- University College London, Department of Cell and Developmental Biology, WC1E 6BT and UCL Consortium for Mitochondrial Research.
2- UCL Institute of Ophthalmology, Bath Street, London EC1V9EL.
3- UCL, Department of Structural and Molecular Biology, London, WC1E 6BT.
4- Departments of Biomedical Engineering and Chemistry, Boston University, MA 02215.
5- Department of Medicine, David Geffen School of Medicine, University of California, Los Angeles, CA 90095.

* - Correspondence to Michael R. Duchen; email – m.duchen@ucl.ac.uk
and Preethi Sheshadri; email – preethi.sheshadri@ukdri.ac.uk

† - Current address - UK Dementia Research Institute, Cardiff University, CF24 4HQ.
# - Current address - Research Centre for Molecular Medicine and Chronic Diseases (CIMUS), Research Health Institute of Santiago (IDIS), University of Santiago de Compostela, Santiago de Compostela, Spain. Networking Research Centre on Neurodegenerative Diseases (CIBERNED), Madrid, Spain.
‡ - Current address - Biofabics, Rua do Campo Lindo, Porto, Portugal.
§ - Current Address - Department of Biomedical and Chemical Engineering, Syracuse University, New York.

Abstract

Background: Heterozygous mutations in the Glucocerebrosidase gene (*GBA1*), which encodes the lysosomal enzyme β-glucocerebrosidase (GCase), are a genetic risk factor for Parkinson's disease (PD). The pathophysiological consequences of *GBA1* mutations on dopaminergic neuronal function, especially their impact on lysosomal function, mitophagy, and mitochondrial bioenergetics, remain unclear.

Methods: Fibroblasts and dopaminergic neurons generated from induced pluripotent stem cells (iPSCs) derived from patients with GBA1-PD were used in the study. Live-cell imaging was performed to measure lysosomal acidification, protease activity, mitochondrial membrane potential, and mitophagy. Mitochondrial morphology and autophagic vesicles were examined using transmission electron microscopy. Oxygen consumption rate was measured by Seahorse assay. V-ATPase assembly was quantified using FLIM-FRET, and pharmacological interventions included rapamycin and acidic nanoparticles. Statistical analyses involved unpaired t-tests, one-way ANOVA, and two-way ANOVA.

Results: GCase activity, lysosomal acidification, protease activity, mitophagy and mitochondrial bioenergetic function were all impaired. Mitochondria were fragmented, with reduced membrane potential and oxygen consumption. MTORC1 was constitutively phosphorylated and FLIM-FRET measurements confirmed impaired lysosomal V-ATPase assembly, which was reversed following rapamycin treatment. Rapamycin and lysosome-targeted acidic nanoparticles rescued lysosomal pH, restored mitophagy, mitochondrial membrane potential and mitochondrial OXPHOS complex levels in *GBA1* mutant dopaminergic neurons.

Conclusions: We reveal a novel mechanistic link between *GBA1* mutations and mitochondrial dysfunction, as disruption of V-ATPase assembly driven by MTORC1 activation impairs lysosomal acidification. Mitophagy is therefore impaired leading to mitochondrial dysfunction, undermining dopaminergic cell function and fate. Pharmacological intervention with rapamycin or acidic nanoparticles restore lysosomal pH and rescue mitochondrial function, signposting a novel therapeutic approach for GBA1-PD.

Keywords: GBA1, Parkinson's Disease, mitochondria, lysosomes, lysosomal pH, MTORC1, acidic nanoparticles

Introduction

Genome-wide association studies have revealed that mutations of the glucocerebrosidase (*GBA1*) gene constitute a significant risk factor in the development of Parkinson's Disease (PD)[1]. The *GBA1* gene encodes the enzyme β-glucocerebrosidase (GCase), which generates glucose and ceramide from glucosylceramide within lysosomes. While homozygous *GBA1* mutations cause Gaucher Disease, which may include a significant neurodegenerative component[2], heterozygous mutations are associated with an increased risk of developing PD. The two most prevalent *GBA1* mutations associated with PD are the N370S and L444P mutations[3]. Intriguingly, the less common E326K mutation in *GBA1* exhibits a relatively mild effect on GCase activity, does not cause Gaucher's Disease, but is correlated with PD risk[4].

Mitochondrial dysfunction appears to constitute a defining characteristic of PD[5]. The adverse impact of dysfunctional mitochondrial oxidative phosphorylation (OXPHOS) on the viability of dopaminergic (DA) neurons is substantiated by experimental models of PD that result from toxins that target complex I[5]. The *Gba1* mouse knockout model, a model of severe neurodegeneration, exhibited severe mitochondrial dysfunction in primary neurons and astrocytes in culture, alongside neurological pathologies associated with PD, including disruption of autophagy-lysosomal pathways, and the accumulation of ubiquitinated proteins and α-synuclein[6].

The autophagosome-lysosome axis and ubiquitin proteasome systems accomplish degradation of dysfunctional organelles and protein degradation and together play a critical role in cellular quality control[7]. Lysosomal acidification generating pH values between 4.5 to 4.7[8] is essential for normal lysosomal function and is required for the activity of lysosomal hydrolytic enzymes and effective protein degradation[44,12]. The acidification is generated by the vacuolar-type H^+ ATPase (V-ATPase), a proton pump composed of a peripheral V_1 domain, which hydrolyses ATP, and a membrane-integrated V_o domain, responsible for the translocation of protons into the lysosomal lumen[10]. Disrupted V-ATPase assembly and V-ATPase dysfunction have been reported associated with multiple disorders[11], including Juvenile-onset Parkinson's Disease[12], Alzheimer's Disease[13,14], Epilepsy[15,16] and Down's syndrome[17].

GBA1-linked pathologies such as Gaucher's disease and PD are associated with a dysfunctional autophagy-lysosome pathway, including impaired lysosomal regeneration from autolysosomes during macroautophagy[18,19]. These investigations suggest that targeting the dysfunctional lysosomal system and the autophagy-lysosome pathway may serve as a potential therapeutic strategy for PD linked to *GBA1* mutations. Although numerous studies indicate that impaired lysosomal acidification plays a role in neuronal pathologies

80 associated with various neurodegenerative disorders[38] and that GBA1-PD is characterised by lysosomal
81 dysfunction [44], the effects of compromised lysosomal acidification in GBA1-PD have not been extensively
82 examined.

83 In this study, we have characterised the consequences of *GBA1* mutations associated with PD for mitochondrial
84 and lysosomal function in patient-derived fibroblasts and DA neurons generated from patient-derived induced
85 pluripotent stem cells (iPSCs). Since GCase is a lysosomal enzyme, we hypothesised that lysosomal dysfunction
86 caused by the mutations might impair mitochondrial function, initiating a pathophysiological cascade culminating
87 in cellular malfunction. We also discovered that constitutive and inappropriate activation of mechanistic target of
88 rapamycin complex 1 (MTORC1) impairs lysosomal acidification by disrupted assembly of the lysosomal V-
89 ATPase complex, resulting in lysosomal dysfunction. Additionally, we demonstrate that restoring lysosomal pH
90 by treatment with rapamycin or acidic nanoparticles (acidic NPs) targeted to lysosomes enhances mitophagy and
91 rescues both lysosomal and mitochondrial function in cells carrying GBA1-PD mutations.

92 **Results**

93 To characterise the impact of PD-related *GBA1* mutations on lysosomal and mitochondrial function, we examined
94 three lines of human dermal fibroblasts and six iPSC lines derived from GBA1-PD patients carrying E326K or
95 N370S mutations, along with two healthy controls. We also included one CRISPR-corrected isogenic control iPSC
96 line each for GBA1-N370S and GBA1-E326K iPSCs. (Table 1). We first performed the experiments in fibroblasts
97 as a proof of principle, and subsequently confirmed the key findings in iPSC-derived DA neurons.

98 **Lysosomal function is impaired in cells with PD-related *GBA1* mutations**

99 As GCase is a lysosomal enzyme, our investigation began by characterising the lysosomes in fibroblasts and DA
100 neurons from both control and PD patient-derived iPSCs. The GBA1 protein expression levels measured by
101 western blot were not significantly different between the control and *GBA1* mutant neurons; however, GCase
102 enzymatic activity was significantly reduced in iPSC-DA neurons and fibroblasts carrying either *GBA1* mutation
103 (Fig 1A, B, S1A, B). Lysosomal acidification was measured using the ratiometric pH-sensitive dye, Lysosensor
104 Yellow/Blue DND160. These data revealed impaired acidification in both E326K and N370S DA neurons and
105 fibroblasts (Fig 1C, S1C, D). Calibration of the lysosomal pH (see methods) gave values of 4.74±0.03 - 4.77±0.02
106 in control cells but between 4.89±0.02 and 5.06±0.03 in the mutant fibroblasts (Fig 1D). The function of endocytic
107 trafficking and lysosomal proteolytic activity was measured using the DQ-Red BSA assay. DQ-Red BSA intensity

was significantly reduced in the *GBA1* mutant neurons, indicating impaired lysosomal degradative function in GBA1-PD cells (Fig 1E, S1E). Autofluorescence excited at 355nm and imaged between 400-600nm showed an unusually bright extramitochondrial component in GBA1-PD fibroblasts (Fig 1F) that was significantly greater than control cells. Spectral scanning and linear unmixing separated the expected mitochondrial NADH signal with an emission peak at 450nm and an extensive non-mitochondrial signal with a peak emission at 480nm, attributed to accumulated lipofuscin. Lipofuscins are cytoplasmic granules generated as a consequence of autophagy and phagocytosis processes, which show auto-fluorescence over a broad spectrum ranging from 480nm to 700nm when excited by ultraviolet or blue light[20]. While the accumulation of lipofuscin serves as an indicator of ageing, abnormal accumulation is consistent with impaired lysosomal acidification and defective autophagy[21]. Accumulation of lipofuscin is also a hallmark of Batten Disease (neuronal ceroid-lipofuscinoses), a severe early-onset neurodevelopmental disorder with progressive neurodegeneration also associated with lysosomal dysfunction [22]. These data collectively indicate significant lysosomal dysfunction in the GBA1-PD cells.

Mitochondria are dysfunctional in cells with GBA1-PD mutations

To determine whether the impaired lysosomal activity in the *GBA1* mutations has a secondary impact on mitochondrial form and function, we measured mitochondrial membrane potential ($\Delta\Psi m$) using the potentiometric fluorescent reporter tetramethyl-rhodamine methyl ester (TMRM). $\Delta\Psi m$ was significantly reduced in E326K and N370S *GBA1* mutant DA neurons and fibroblasts (Fig 2A, S2A, C). The lower $\Delta\Psi m$ was accompanied by mitochondrial fragmentation in the N370S and E326K DA neurons and fibroblasts (Fig 2Aii c,d, S2Aii b). Ultrastructure analysis using electron microscopy revealed significant differences in mitochondrial morphology in the *GBA1* mutant neurons, including reduced cristae density and increased mitochondrial area, along with decreased mitochondrial aspect ratio, indicating mitochondrial swelling and fragmentation in the *GBA1* mutant iPSC DA neurons (Fig. 2B). Measurements of oxygen consumption rates using the 'Seahorse' respirometry system revealed ~40% decrease in basal oxygen consumption rate in the *GBA1* mutant DA neurons with the isogenic controls (Fig 2C). To exclude changes in mitochondrial mass and to explore the substrate dependence of mitochondrial respiration, we used mitochondria isolated from the cultures. This allowed measurements of respiratory rates with different substrates, favouring complex I (pyruvate/malate) or complex II (rotenone/succinate). ADP-stimulated respiration (State 3) rate using both CI and CII-dependent substrates was significantly reduced in the *GBA1* mutant neurons compared to the control neurons (Fig 2D, S2C). Western Blots of the OXPHOS complex proteins using a cocktail of antibodies to respiratory chain proteins, revealed a

137 significant increase in the expression of complex IV in E326K DA neurons (Fig 2Eii a and S2Dii a) and increased
138 expression of complex I proteins in N370S neurons compared to the isogenic controls (Fig 2Eii b and S2Dii b).
139 Complex III was reduced in both E326K and N370S DA neurons compared to the isogenic controls while the
140 expression of other respiratory chain proteins remained unaltered. None of these data suggested any defect in
141 complex I assembly or function. These data collectively point to impaired mitochondrial bioenergetic function in
142 fibroblasts and neurons carrying *GBA1* mutations.

143 **Mitophagy is impaired in cells with GBA1-PD mutations**

144 We then set out to explore the underlying mechanisms that link impaired lysosomal function to impaired
145 mitochondrial bioenergetics in the GBA1-PD fibroblasts and DA neurons. A logical mechanism linking impaired
146 lysosomal function with mitochondrial dysfunction might operate through dysfunctional mitophagy and our
147 earlier work also established dysfunctional mitophagy in *Gba1* KO mice[6]. We quantified mitophagy using the
148 dual excitation probe mt-Keima (Fig 3A). mt-Keima is a pH-sensitive probe that measures the fraction of
149 mitochondria in neutral (pH 7 - 7.8 in the mitochondrial matrix) versus acidic pH (pH 4.5-4.7 in lysosomes)
150 environment[23]. The mt-Keima signal ratio was significantly reduced in fibroblasts and DA neurons in the
151 fibroblasts and DA neurons carrying both the GBA1-N370S and GBA1-E326K mutations indicating impaired
152 mitophagy (Fig 3Aii. S3Aii, Bii). Western blotting to quantify the status of autophagy pathways in the *GBA1*
153 mutant neurons revealed increased LAMP1 levels in E326K and N370S neurons, along with increased
154 pMTORC1/MTORC1 ratio in the two mutant types. While LC3 flux, and expression of p62 and TOM20 were
155 increased in the E326K mutant iPSC DA neurons, these were not significantly altered in the N370S DA neurons
156 (Fig 3B). Since the lysosomal pH is increased in GBA1-PD cells (Fig 1D), the reduced mt-Keima signal in GBA1-
157 PD cells could be attributed either to the altered lysosomal pH or to the impaired fusion of autophagosomes to
158 lysosomes. To address this, we performed triple staining of fibroblasts against citrate synthase (CiS, for
159 mitochondria), LAMP1 (for lysosomes), and LC3 (for autophagosomes). Subsequent imaging revealed that
160 although there was no significant difference in mitophagosome (mitochondria and autophagosome colocalisation)
161 density between *GBA1* mutant and control fibroblasts, mitolysosome (colocalisation of mitochondria and
162 lysosomes) density was significantly increased in the *GBA1* mutant fibroblasts (Fig 3C). Characterisation of
163 electron micrographs for specific autophagic vesicle types based on Neikirk et al.,2023[24], showed that
164 autophagic vesicles, specifically the autolysosome and lysosome number, were significantly increased in both
165 *GBA1* mutant fibroblasts and neurons. (Fig 3Dii, S3Cii a and b). From the micrographs, the autophagosomes also

166 appeared to be fully enclosed, ruling out incomplete phagophore formation as the underlying mechanism of
167 autophagy defect. These data indicated that mitophagy is significantly impaired in cells carrying the GBA1-PD
168 mutations and the decrease in mitophagy is likely due to impaired pH and not improper phagophore formation.

169 **V-ATPase complex formation is impaired in GBA1-PD**

170 Since our data showed an accumulation of lysosomes and autolysosomes in GBA1-PD fibroblasts and iPSC-DA
171 neurons, we suspected this was a result of impaired lysosomal acidification. Assembly of the pH regulatory
172 component in lysosomes – the Vacuolar-type H+ ATPase (V-ATPase) is regulated by MTORC1[25], which was
173 constitutively phosphorylated in the GBA1-PD mutant cells. Ratto et al.[25] demonstrated that under nutrient-
174 deprived conditions, MTORC1 is inactive and is distributed in the cytosol, enabling the peripheral ATP6V_1 to bind
175 to the membrane-bound ATP6V_0 domain, forming a functional V-ATPase complex allowing proton exchange and
176 acidification of the lysosomes.

177 Under nutrient-rich conditions, MTORC1 is phosphorylated and remains on the lysosomal membrane, preventing
178 the formation of a functional V-ATPase complex[25]. While the V-ATPase maintains lysosomal pH, disruption of
179 the complex does not hamper autolysosome formation[26]. Total protein estimation through western blotting
180 revealed no significant difference in the expression of ATP6V_0D2 and ATP6V_1A or ATP6V_1H between the control
181 and mutant DA neurons (Fig 4A). To examine their expression levels specifically in lysosomes, we performed a
182 lysosomal enrichment assay and probed for pMTORC1, LAMP1, and the ATP6V_0 and ATP6V_1 components (Fig
183 4Bi). Equal amounts of cell lysate and purified lysosomes (25mg) were used to run the western blots. LAMP1
184 was used as a marker to verify lysosomal enrichment and GAPDH was used as a marker for cell lysates (Fig 4Bi).
185 For quantification (Fig 4Bii), the bands in the lysosome-enriched samples were normalised to the protein levels
186 in the lysosome-enriched samples from untreated isogenic controls. Since pMTORC1 represents the active form
187 of MTORC1 and is found on the lysosomal membrane, we measured only pMTORC1 levels. pMTORC1
188 expression was increased up to two-fold, and LAMP1 expression was increased ~1.5 fold in the GBA1-mutant
189 DA neurons. However, ATP6V_1A expression was reduced by ~40% and ATP6V_1H by ~15% within the lysosomes
190 fractionated from *GBA1* mutant DA neurons, while ATP6V_0D2 levels remained unchanged between the control
191 and mutant iPSC-DA neurons (Fig 4Bii). Furthermore, overnight treatment of *GBA1* iPSC-DA neurons with the
192 MTORC1 inhibitor rapamycin (200nM) decreased the pMTORC1 and LAMP1 levels, while increasing ATP6V_1A
193 and ATP6V_1H expression in the lysosomes and the ATP6V_0D2 levels remained constant (Fig 4Bi b and Bii).

194 In order to assess the V-ATPase assembly, we transfected the control and *GBA1* mutant fibroblasts with
195 ATP6V_1B2-mNeongreen and ATP6V_0a3-mScarlet and quantified their FRET interaction using fluorescence
196 lifetime imaging microscopy (FLIM)[27]. The data were best fit to a biexponential decay function. The ATP6V_0a3
197 construct utilises the more rapidly maturing but photophysically heterogeneous acceptor variant mScarlet-I[28].
198 This exhibits at least two fluorescence lifetimes, meaning the biexponential decay of the donor is an
199 oversimplification given the likelihood of contrasting FRET rates to each acceptor species [29,30]. The results are
200 therefore presented as the mean (amplitude weighted) fluorescence lifetime -τ_m- which will nevertheless respond
201 to variations in FRET without having to interpret the meaning of individual decay components and amplitudes.
202 τ_m of ATP6V_1B2-mNeongreen averaged 617.72± 25.3 ps in control fibroblasts but increased to 760.88± 20.36 ps
203 in N370S and 811.03± 17.04 ps in E326K mutant fibroblasts, indicating an increased distance between
204 ATP6V1B2-mNeongreen and ATP6V0a3-mScarlet signalled by a reduction in FRET. Overnight treatment with
205 200nM rapamycin significantly decreased τ_m to 652.7± 19.69 ps and 726.05± 21.2 ps in E326K and N370S
206 fibroblasts respectively while the τ_m control fibroblasts was at 590.5± 32.7 ps (Fig 4C). To validate the subcellular
207 localisation process within a condensed timeframe, we administered 1 μM rapamycin to the cells and performed
208 FLIM every 10 minutes for 40 minutes. The mean fluorescence lifetime of ATP6V1B2-mNeongreen exhibited a
209 progressive decline in the *GBA1* mutant fibroblasts, decreasing from ~850 ps at 0 min to ~580 ps at 40 minutes,
210 while τ_m in control fibroblasts showed only a small reduction, decreasing from ~675 ps at 0 min to ~588 ps at 40
211 minutes (Fig 4Dii). The FLIM-FRET data thus confirmed impaired assembly of the V -ATPase complex in *GBA1*
212 mutant cells.

213 All these data are consistent with a model in which phosphorylation of MTORC1 at the lysosome membrane limits
214 the formation of a functional V-ATPase complex in the GBA1-PD cells. Employing rapamycin as a potent
215 MTORC1 inhibitor reduced MTORC1 activity and facilitated the formation of a functional V-ATPase complex.

216 **Acidification of lysosomes is sufficient to restore lysosomal, mitochondrial function and mitophagy in**
217 **GBA1-PD**

218 Our data show that *GBA1* mutations lead to significantly impaired lysosomal acidification and mitophagy and
219 suggest that this failure of cellular homeostasis may underlie the mitochondrial dysfunction seen in GBA1-PD
220 cells. We therefore wondered whether restoring lysosomal pH could rescue these defects in GBA1-PD cells. Since
221 impaired V-ATPase complex formation may be a consequence of MTORC1 hyperphosphorylation, we explored
222 the impact of treatment with rapamycin (overnight treatment with 200nM) on lysosomal and mitochondrial

223 function. As an independent pH modulator, we employed novel poly(ethylene tetrafluorosuccinate-co-succinate)
224 nanoparticles (NPs), which acidify lysosomes[31].

225 We first validated the effects of rapamycin and the nanoparticles in patient-derived fibroblasts (Fig S4). To confirm
226 that the NPs were localised to the lysosomes, we loaded the fibroblasts with rhodamine-tagged NPs and stained
227 the cells with Lysotracker blue DND22 (Fig S4A) which confirmed the localisation of the NPs to lysosomes.
228 Overnight treatment with 180 µg/mL acidic NPs composed of poly(ethylene tetrafluorosuccinate-co-succinate)
229 restored lysosomal pH in *GBA1* mutant cells to levels comparable to those of control fibroblasts as measured using
230 the pH-sensing ratiometric probe Lysosensor Yellow/Blue DND160. Treatment with non-acidic control NPs did
231 not significantly affect the lysosomal pH in the *GBA1* mutant fibroblasts (Fig. S4B, C). TMRM staining
232 demonstrated that both rapamycin and the acidic NPs significantly rescued the ΔΨm in the mutant fibroblasts (Fig
233 S4F, G). We also found that the ΔΨm was increased in control 2 and E326K fibroblasts upon control NP treatment
234 (Fig S4G). We wondered whether the effect of control NPs on ΔΨm could be due to the succinate component in
235 the poly(ethylene succinate) control NPs. However, treatment with 3mM Diethyl Succinate for 30 minutes did not
236 have any effect on the ΔΨm in control and *GBA1* mutant fibroblasts (Fig S4H).

237 We then assessed the impact of rapamycin and acidic NPs on *GBA1* mutant iPSC-derived DA neurons (Fig 5).
238 Treatment with 200nM rapamycin and 180 µg/mL acidic NPs restored lysosomal pH, ΔΨm, and mitophagy in the
239 E326K and N370S iPSC DA neurons (Fig 5A, B, C). Although there was no change in GBA1 expression levels,
240 GCase activity was increased in *GBA1* mutant DA neurons following treatment with either rapamycin or acidic
241 NPs (Fig S4 D, E). Additionally, western blotting of OXPHOS complexes indicated that the increased
242 mitochondrial complex IV levels in E326K DA neurons and the reduced complex I levels in the N370S DA
243 neurons were normalised upon treatment with either rapamycin or acidic NPs. Complex III levels were also
244 rescued upon rapamycin or acidic NPs treatment in both E326K and N370S DA neurons (Fig S4I).

245 As rapamycin restores the assembly of the V-ATPase complex in *GBA1* mutant cells (Fig 4D-F), we asked whether
246 the acidic NPs also function through the V-ATPase complex formation. FLIM-FRET experiments conducted on
247 control and acidic NP-treated *GBA1* mutant fibroblasts transduced with ATP6V_1B2-mNeongreen and ATP6V_0a3-
248 mScarlet plasmids demonstrated a further increase in the τ_m of ATP6V1B2 in both control and mutant fibroblasts
249 treated with acidic NPs, confirming that the acidic NPs operate independently of V-ATPase (Fig S4J).

250 Thus, the data presented here suggest that constitutive phosphorylation of MTORC1 in GBA1-PD cells leads to
251 impaired lysosomal pH and compromised lysosomal proteolytic function. This results in the accumulation of

252 mitolysosomes and impaired mitophagy. The compromised mitophagy culminates in mitochondrial dysfunction
253 in *GBA1* mutant cells. Furthermore, inhibiting MTORC1 activity or pharmacologically decreasing lysosomal pH
254 using acidic NPs enhances lysosomal proteolytic activity, rescuing mitochondrial dysfunction in *GBA1* mutant
255 iPSC-DA neurons and fibroblasts.

256 **Discussion:**

257 We report a range of abnormalities in the lysosomes and mitochondria of GBA1-PD fibroblasts and iPSC-DA
258 neurons carrying E326K or N370S *GBA1* mutations. Given that GBA1 is a lysosomal-resident protein, we
259 hypothesised that mitochondrial dysfunction is likely to reflect a primary lysosomal defect. We used the
260 ratiometric probe Lysosensor Yellow/Blue DND 160 to measure lysosomal pH. When calibrated, these
261 measurements revealed that lysosomal pH in control cells ranged from 4.74 ± 0.03 to 4.77 ± 0.02, while in mutant
262 cells it showed a significant shift to a range of 4.89 ± 0.02 to 5.06 ± 0.03. Reports in the literature indicate that
263 the optimal pH for lysosomal function ranges between 4.2 and 4.8, depending on the cell type [8,32]. Although
264 the difference between control and mutant cells seems modest, the data we present suggest that this difference in
265 mutant cells is functionally significant. In line with other studies, we observed a pH-dependent decrease in the
266 lysosomal enzyme activity, an increase in lysosomal number, and disruption of mitophagy and mitochondrial
267 metabolism [18,33–39].

268 Very few reports discuss mitochondrial abnormalities associated with GBA1-PD [35,40–43], and even fewer
269 explore the status of mitophagy pathways mitophagy [44]. The TMRM data indicated reduced ΔΨm and also
270 revealed mitochondrial fragmentation. EM experiments supported these findings, where mitochondria were
271 shorter, swollen, and mitochondrial aspect ratio was reduced compared to controls. These data, along with reduced
272 density of cristae, collectively indicate structural abnormalities in the mitochondria. A decline in ΔΨm is known
273 to destabilise inner membrane organisation and promote both swelling and fragmentation[45], which aligns with
274 the morphological shift toward more rounded, fragmented mitochondria observed in our analyses. We also found
275 a significant reduction in basal respiratory rates and substrate-dependent mitochondrial respiration in the E326K
276 and N370S DA neurons. The compromised bioenergetics and structural abnormalities collectively indicate
277 dysfunctional mitochondria. Mitochondrial complex III levels were reduced in GBA1-E326K and N370S DA
278 neurons compared to the respective isogenic controls, quantified in western blots. Mitochondrial complex III plays
279 a key role in driving respiration and maintenance of membrane potential [46] and so reduced expression of
280 complex III could account for the reduced mitochondrial membrane potential and reduced respiratory rate in

GBA1-PD DA neurons. Reduced mitochondrial complex III expression has also been reported in platelets and lymphocytes of PD patients[47,48]. However, increased complex IV levels were observed in only two E326K mutant DA neurons, while one N370S line exhibited increased complex I expression. This could be due to variation between subjects. More replications and other experiments need to be performed to obtain conclusive data on mitochondrial complex levels in the E326K and N370S GBA1-PD lines. Mitochondrial dysfunction was also associated with impaired mitophagic flux in E326K and N370S GBA1-PD fibroblasts and iPSC-DA neurons.

Numerous studies have suggested mechanistic evidence for a connection between PD and *GBA1* mutations. For example, dysfunctional mitochondria in primary neurons and astrocytes were described in the *Gba1* mouse knockout model, associated with an impaired autophagy-lysosomal pathway, resulting in the accumulation of ubiquitinated proteins and α-synuclein[6]. Various studies have explored the mechanisms behind the PD pathology in *GBA1* mutant models. A recent study emphasised that decreased GCase activity in GBA1-PD midbrain dopaminergic neuronal cells leads to defective modulation of the untethering protein TBC1D15, which regulates Rab7 GTP hydrolysis for contact untethering. This impairment results in prolonged mitochondria-lysosome contacts, potentially affecting mitochondrial dynamics and function in GBA1-linked PD[42]. Baden et al. proposed an alternative function of GBA1 in the mitochondria in maintaining the integrity of complex I and support of energy metabolism[40], although in the present study we found no evidence for mitochondrial localisation of GBA1 nor impaired assembly of complex I.

Respirometry assays using isolated mitochondria revealed a marked reduction in both maximal respiratory capacity and ATPase-linked oxygen consumption in GBA1-E326K and N370S mutant DA neurons, upon stimulation with complex I (pyruvate/malate) and complex II (rotenone/succinate) substrates. The impairment across both complexes points to a global mitochondrial dysfunction, potentially arising from structural abnormalities such as fragmented mitochondria and decreased cristae density—features observed in these mutants—or as a downstream consequence of lysosomal dysfunction. Notably, lysosome-related mitochondrial impairment has also been reported in Tre-2/Bub2/Cdc16 (TBC1) domain containing Kinase (TBCK) encephaloneuronopathy, supporting a broader link between lysosomal defects and mitochondrial pathology[49].

Recent evidence suggests that the primary cause of the pathologies associated with lysosomes and mitochondria in PD is the *GBA1* mutation. There appears to be a correlation between the onset of PD and lysosomal dysfunction caused by impaired GCase activity. Dysfunctional lysosomes disrupt cellular signalling networks, metabolic processes, autophagy, and the regulation of calcium (Ca^{2+}) signalling, all of which may contribute to PD

310 pathology[7,10,19,36,38]. Furthermore, both lysosomal function and autophagy are intrinsically dependent on
311 lysosomal acidification, which is influenced by the pH-dependence of lysosomal enzyme activity and substrate
312 degradation, as well as the regulation of lysosomal calcium efflux[50]. Li et al. also suggest that autophagy in
313 L444P mutant GBA1-PD neurons is impaired at two stages: the initial autophagy stage and the lysosomal
314 degradation stage. While these reports indicate a relationship between *GBA1* mutations and autophagic,
315 lysosomal, and mitochondrial dysfunction, a mechanistic dissection of these multi-organellar dysfunctions is
316 lacking.

317 Dysregulation of the MTORC1 pathway is reported in various neurodegenerative diseases, including PD and
318 Alzheimer's disease[51,52]. A recent study by Chen et al. suggests that hyperphosphorylation of MTORC1 in
319 striatal inhibitory neurons diminishes the disruption of dopamine receptor activity, alongside odour preference, in
320 transgenic mice [53]. Liu et al. demonstrate the role of MTORC1 in dopamine dynamics and synaptic
321 plasticity[54]. These results elucidate the additional impacts of increased phosphorylated MTORC1 on PD.
322 Kaempferol, an MTORC1 inhibitor, has also been shown to promote autophagy and to protect DA neurons in the
323 MPTP-induced C57BL/6J–PD mouse model [55]. All this literature suggests that hyperphosphorylated MTORC1
324 may play a central role in the development of PD associated with *GBA1* mutations. Our study also indicates
325 increased MTORC1 phosphorylation in GBA1-PD fibroblasts and iPSC-DA neurons. While the link between
326 MTORC1 hyperphosphorylation and *GBA1* mutations is unclear, it may reflect a cellular stress response to lipid
327 substrate accumulation under *GBA1* mutant conditions[56–58].

328 Recent evidence underscores the significance of impaired lysosomal acidification in various disease processes.
329 Notably, impaired lysosomal acidification is proposed to be a critical factor in the pathogenesis of multiple
330 neurodegenerative diseases[13, 24, 27, 56]. Mutations in presenilin-1 (*PS1*) associated with familial Alzheimer's
331 disease have been demonstrated to inhibit the lysosomal acidification of human *PS1* mutant fibroblasts, resulting
332 in chronic alterations in autophagy and degradation, which may be restored through lysosomal reacidification[59].
333 Furthermore, it has been established that individuals with Down Syndrome, who are predisposed to early-onset
334 dementia resembling Alzheimer's disease, exhibit increased levels of the β-cleaved carboxy-terminal fragment of
335 the amyloid precursor protein due to the presence of an additional chromosome 21, which impairs lysosomal
336 acidification and functionality via the inhibition of V-ATPase[17]. Collectively, these studies illuminate the
337 connections between the impairment of lysosomal acidification in autophagic pathways and the pathogenesis of
338 neurodegeneration, thereby presenting potential therapeutic avenues for targeting lysosomal function and pH to
339 mitigate these debilitating diseases. Acidic NPs in the form of poly(lactic-co-glycolic acid) (PLGA) acidic NPs

340 have been previously used to reduce lysosomal pH and disease progression in cells derived from GBA1-N370S
341 PD patient fibroblasts and in PD mouse models[61]. Additionally, poly-succinate acidic NPs used in this study
342 have been employed to restore lysosomal pH and rehabilitate metabolic and lysosomal functions in cases of non-
343 alcoholic fatty liver disease[31].

344 As an MTORC1 inhibitor[62], rapamycin also acts as a prominent inducer of mitophagy and has been
345 demonstrated to mitigate mitochondrial dysfunction in various disease models through inhibition of the MTORC1
346 pathway[63,64]. Consistent with findings from other studies, we found that rapamycin rescues mitophagy and
347 mitochondrial function in GBA1-PD fibroblasts and DA neurons. This could either be due to the role of MTORC1
348 as a regulator of mitochondrial function[65,66] or a downstream effect of lysosomal acidification by MTORC1
349 inhibition. To establish whether impaired lysosomal acidification is the cause of these dysfunctions, we employed
350 an independent pH modulator in the form of novel acidic poly-succinate NPs, which rectify lysosomal pH in the
351 cells while enhancing lysosomal and mitochondrial functions in GBA1-PD fibroblasts and DA neurons. Our data
352 confirmed the efficacy of acidic NP treatment on lysosomal pH *in vitro*. We show that the ratio of alkaline vs
353 acidic lysosomes decreased significantly in all mutants and most controls after the acidic NP treatment,
354 demonstrating a decrease in mean lysosomal pH. The effect on controls could be due to the alkalinisation of the
355 lysosomes with age, which can be reversed by the acidic NP treatment in healthy cells[67]. Importantly, treatment
356 with acidic NP successfully eliminated the differences in lysosomal pH between the *GBA1* mutants and the
357 controls. We conclude that the restoration of lysosomal acidification in the mutant cells improved lysosomal
358 function.

359 Lysosomal acidification also rescued GCase activity in the cells despite mutations in the GBA1 protein. Other
360 studies have also demonstrated the restoration of GCase activity despite *GBA1* mutations under acidic pH
361 conditions[68–70]. The N370S mutation results in a structurally rigid protein with reduced intra-lysosomal
362 stability and reduced GCase activity[70], and the E326K mutation has little effect on the active catalytic site of
363 the protein but affects the dimerisation and quaternary structure formation due to folding defects, likely leading
364 to a mild reduction in GCase activity at higher pH levels[68]. GCase activity depends on protonation of amino
365 acids at the active sites and due to interaction of the protein with activators like saposin C[71], which is affected
366 due to the mutation[68,72]. Restoring the acidic pH in the lysosomes helps restore functional GCase activity
367 despite the mutations possibly by stabilising protein structure, improving folding and optimising the active-site
368 ionisation[68,73]

369 To explore whether altered lysosomal pH is related to mitochondrial dysfunction in GBA1-PD, we evaluated
370 ΔΨm, redox levels, and oxidative phosphorylation (OXPHOS) protein levels following treatment with NPs. Our
371 results reveal a significant rescue of ΔΨm among GBA-PD mutants after acidic NP treatment, indicating improved
372 mitochondrial function. When compared to untreated healthy controls, the difference in ΔΨm was no longer
373 statistically significant in the mutants following treatment with acidic NPs. It is noteworthy that some control
374 samples also exhibited alterations due to acidic NP treatment, resulting in a small but significant increase in ΔΨm.
375 We also found a significant increase in ΔΨm in control 2 and E326K fibroblasts upon control NP treatment. Since
376 the NPs are composed of poly(ethylene-succinate), we suspected this could be a substrate-mediated (succinate)
377 effect in control NP treated conditions. However, 30-minute treatment with 3mM Diethyl Succinate did not alter
378 the ΔΨm in the control or mutant fibroblasts. Acidic NP treatment also rescued the differential mitochondrial
379 complex levels observed in the GBA1-E326K and N370S DA neurons. Rescuing lysosomal pH also improved
380 mitophagy in the GBA1-PD fibroblasts and iPSC-DA neurons.

381 **Conclusions:**

382 We have explored the relationship between lysosome biology, pH, mitophagy and mitochondria in cells carrying
383 PD-associated mutations of *GBA1*. A detailed examination of the pathophysiology of these cells reveals a range
384 of abnormalities in the lysosomes, including reduced GCase activity, an increased lysosomal number, impaired
385 lysosomal acidification, and impaired pH-dependent lysosomal proteolytic activity. Mitochondrial dysfunction is
386 reflected by reduced ΔΨm, swollen, fragmented mitochondria, decreased cristae density, and the accumulation of
387 abnormal mitochondria, along with a reduced oxygen consumption rate. We also found a decrease in mitophagy
388 and an accumulation of autolysosomes in the GBA1-PD cells. We show that increased pMTORC1 on the
389 lysosomal membrane, possibly due to nutrient accumulation, hinders the formation of a functional V-ATPase
390 complex in GBA1-PD cells, thereby compromising lysosomal acidification. We found that inhibiting MTORC1
391 using rapamycin rescues functional V-ATPase formation and lysosomal pH in the GBA1-PD neurons, along with
392 mitophagy and mitochondrial function. Independent modulation of lysosomal pH using acidic poly-succinate NPs,
393 restored lysosomal pH, rescued mitophagy and restored mitochondrial function in the GBA1-PD fibroblasts and
394 iPSC-DA neurons (Fig 6). Since rapamycin has broad effects, the comparison to NPs is valuable, adding a
395 translational value for future applications. These studies identify the underlying mechanism causing impaired
396 lysosomal pH regulation associated with PD-related GBA1 mutations and provide evidence that restoring
397 lysosomal pH is sufficient to rescue lysosomal function, to restore mitophagy and therefore to rescue

398 mitochondrial function in both GBA1-PD patient-derived fibroblasts and iPSC-DA neurons. We highlight that
399 lysosomal pH correction is a pivotal, unifying therapeutic target in GBA1-PD.

400 **Figure legends:**

401 **Figure 1: Lysosomal abnormalities in GBA1-PD DA cells-** Representative western blot images of GBA1 protein
402 expression (Ai) and quantification (Aii a,b) in isogenic control and GBA1-E326K and N370S DA neurons. GCase
403 activity in GBA1-E326K (Bi a) and GBA1-N370S (Bi b) DA neurons and respective isogenic controls.
404 Representative ratioed images (Ci a, b) and quantification of fluorescence ratio of GBA1-E326K (Cii a) and
405 GBA1-N370S (Cii b) DA neurons and respective isogenic controls labelled with Lysosensor Yellow/Blue DND
406 160, indicating lysosomal pH in cells. D) Histogram depicting mean lysosomal pH values in *GBA1* mutant
407 fibroblasts. Representative confocal images (Ei a,b) and quantification of relative intensity of GBA1-E326K (Eii
408 a) and GBA1-N370S (Eii b) DA neurons and respective isogenic controls stained with DQ-Red BSA indicative
409 of proteolytic activity. Representative confocal images (Fi) and quantification (Fii) of lipofuscins in GBA1
410 fibroblasts, which are seen upon autofluorescence. Data represented as mean±SD; one-sample Wilcoxon rank t-
411 test, unpaired t-test or One-way ANOVA with Kruskal-Wallis and Dunn's multiple comparisons test. p-values are
412 noted on the graphs; the statistical tests, corresponding effect sizes, and confidence intervals for each graph are in
413 supplementary table 2.

414 **Figure 2: Mitochondrial dysfunction in GBA1-PD DA neurons:** Representative confocal images of GBA1-
415 E326K (Ai a) and GBA1-N370S (Ai b) DA neurons along with isogenic controls stained with TMRM and
416 subsequent quantification of fluorescent intensity to measure $\Delta\Psi m$ (Aii a, b) and mitochondrial fragmentation
417 count (Aii c,d). Representative ultramicroscopic images of isogenic control and GBA1-E326K (Bi a) and GBA1-
418 N370S (Bi b) DA neurons. Bii– Box-and-whisker plots showing the minimum, maximum, median, and
419 interquartile range of the log(Y) values of the morphological parameters - average number of mitochondria(a, e),
420 average cristae density in mitochondria (b, f), average mitochondrial area (c, g) and mitochondrial aspect ratio (d,
421 h). The white arrow indicates normal mitochondria; the black arrow indicates abnormal mitochondria. Histograms
422 representing the basal respiration rate in *GBA1* mutant iPSC-DA neurons from GBA1-E326K (C a) and GBA1-
423 N370S mutant lines(C b) and respective isogenic controls. Representative seahorse plots showing oxygen
424 consumption rates in iPSC-DA neurons from GBA1-E326K (Di a) and GBA1-N370S (Di b) DA neurons and
425 respective isogenic controls, using various substrates. Histograms representing State 3(ATP Production) in
426 mitochondria isolated from GBA1-E326K (Dii a) and GBA1-N370S (Dii b) DA neurons and isogenic controls,
427 as measured by seahorse assay. E i and ii) Representative immunoblotting images (Ei) with subsequent

428 quantification of OXPHOS complex proteins in GBA1 E326K (Eii a) and N370S (Eii b) DA neurons. Data
429 represented as mean±SD; Statistics: Mann-Whitney's test, log-transformed and unpaired t-test, one-sample
430 Wilcoxon rank test or Ordinary two-way ANOVA with Šidák multiple comparisons test with single pooled
431 variance. p-values are noted on the graphs. The statistical tests, corresponding effect sizes, and confidence
432 intervals for each graph are reported in supplementary table 2.

433 **Figure 3: Mitophagy defects in GBA1-PD DA neurons:** Representative images of GBA1-E326K (Ai a)and
434 GBA1-N370S (Ai b) DA neurons and isogenic controls transduced with mt-Keima plasmid and imaged with
435 excitation at 458 and 543nm and subsequent quantification of the ratio of signals at 543/458nm (Aii a,b).
436 Representative western blot images of *GBA1* mutant and isogenic control lysates probed for autophagic proteins
437 (Bi) and subsequent quantification of protein levels (Bii a,b) Representative Immunofluorescence images of
438 control and N370S fibroblasts probed against Citrate Synthase (CiS), LAMP1 and LC3, labelling mitochondria,
439 lysosomes and autophagosomes respectively (Ci) and subsequent quantification of colocalisation co-efficient of
440 mitophagosomes (Cii a) and mitolysosomes(Cii b). Representative TEM images (Di) and quantification (Dii) of
441 control and E326K mutant fibroblasts capture different autophagy phases in the cells. Black arrows may indicate
442 protein aggregates, yellow arrows indicate autolysosomes, red arrows indicate autophagosomes, and green arrows
443 indicate lysosomes in the cells. Data represented as mean±SD; Statistics: Mann-Whitney's test, one-sample
444 Wilcoxon rank test, One-way ANOVA with Holm-Šidák multiple comparisons test or Ordinary two-way ANOVA
445 with Šidák multiple comparisons test. p-values are noted on the graphs. The statistical tests, corresponding effect
446 sizes, and confidence intervals for each graph are in supplementary table 2.

447 **Figure 4: Impaired V-ATPase complex formation in GBA1-PD cells-** Representative images of western blots
448 (Ai) and quantification of protein levels in total cell lysates from isogenic control and GBA1-E326K (Aii a) and
449 GBA1-N370S (Aii b) mutant DA neurons probed against LAMP1 and V-ATPase complex proteins. Representative
450 immunoblotting images of cell supernatant and lysosomes separated by lysosome enrichment assay in untreated
451 (Bi a) and 200nM rapamycin-treated (Bi b) GBA1-PD DA neurons and isogenic controls, and subsequent
452 quantification (Bii) of V-ATPase complex proteins and pMTOR. Representative FLIM images of ATP6V_1B2-
453 mNeonGreen in control and GBA1-PD fibroblasts co-transfected with ATP6V_0a3-mScarlet and treated
454 with/without 200nM rapamycin (Ci) and subsequent quantification of mean lifetime (τ_m) (Cii b). Cii a)
455 Representative decay plots and exponential fit of ATP6V1B2-mNeongreen in the Control and N370S and E326K
456 mutant fibroblasts. D i) Time point images of ATP6V_1B2-mNeongreen in control and GBA1-PD fibroblasts co-
457 transfected with ATP6V_0a3-mScarlet and treated with 1 μM rapamycin and imaged over a period of 40 mins and

458 subsequent quantification of τ_m shown in Dii) Data represented as mean±SD; Statistics: one-sample Wilcoxon
459 rank test or Ordinary two-way ANOVA with Tukey's multiple comparisons test with single pooled variance. p-
460 values are noted on the graphs. The statistical tests, corresponding effect sizes, and confidence intervals for each
461 graph are in supplementary table 2.

462 **Figure 5: Rapamycin and acidic NPs rescue lysosomal and mitochondrial dysfunction in *GBA1* mutant DA**
463 **neurons:** Representative ratioed images of GBA1-E326K (Ai a) and GBA1-N370S (Ai b) DA neurons and
464 respective isogenic controls treated overnight with 200nM rapamycin or 180µg/mL acidic NPs and stained with
465 Lysosensor Yellow/Blue DND 160 (Ai a,b) and quantification of fluorescence ratio (Aii a-d) indicating lysosomal
466 pH. Representative confocal images of GBA1-E326K (Bi a) and GBA1-N370S (Bi b) DA neurons and respective
467 isogenic controls treated with 200nM rapamycin or 180µg/mL acidic NPs and stained with TMRM to measure
468 changes in ΔΨm (Bii a-d). Representative confocal Images of GBA1-E326K (Ci a) and GBA1-N370S (Ci b) DA
469 neurons and respective isogenic controls treated with 200nM rapamycin or 180µg/mL acidic NPs and probed with
470 mt-Keima plasmid and imaged with excitation at 458 and 543nm and subsequent quantification of the ratio of
471 signals at 543/458nm (Cii a-d). Data represented as mean±SD; Statistics: Ordinary two-way ANOVA with
472 Uncorrected Fisher's LSD with single pooled variance. p-values are noted on the graphs. The statistical tests,
473 corresponding effect sizes, and confidence intervals for each graph are in supplementary table 2.

474 **Figure 6: Cartoon to illustrate the proposed pathophysiological cascade in GBA1-related Parkinson's**
475 **Disease and how the phenotype can be corrected by targeting lysosomal pH -** GBA1-PD cells exhibit a range
476 of abnormalities in lysosomal biology, including reduced GCase activity, increased lysosomal numbers, elevated
477 lysosomal pH, and decreased pH-dependent proteolytic activity. Mitochondrial dysfunction is evidenced by a
478 decreased ΔΨm, decreased oxygen consumption rate, swollen mitochondria, reduced cristae density, and the
479 accumulation of abnormal mitochondria. Mitophagy is suppressed and autolysosomes accumulate within the
480 GBA1-PD cells. Restored acidification of lysosomes with rapamycin or acidic poly-succinate NPs enhances
481 lysosomal function and improves mitophagy, thereby rescuing mitochondrial dysfunction in GBA1-PD fibroblasts
482 and lysosomes.

483 **Supplementary Figure 1: Lysosomal abnormalities in GBA1-PD DA neurons and fibroblasts-** GBA1 protein
484 expression (Ai) and subsequent quantification of GBA1 levels in control and GBA1-E326K (Aii a) and N370S
485 (Aii b) DA neurons. GCase activity in GBA1-E326K (Bi a) and GBA1-N370S (Bi b) DA neurons and fibroblasts
486 (Bii). Representative ratioed images of GBA1-E326K and GBA1-N370S fibroblasts (Ci) and DA neurons (Di a,b)
487 stained with Lysosensor Yellow/Blue DND 160, subsequent quantification of fluorescence ratio measuring

488 lysosomal pH (Cii, D ii a,b). Histogram representing quantification of DQ-Red BSA intensity in GBA1-E326K
489 (E a) and GBA1-N370S (E b) and control DA neurons indicating lysosomal proteolytic activity. Data represented
490 as mean±SD; one-sample Wilcoxon rank t-test or One-way ANOVA with Kruskal-Wallis and Dunn's multiple
491 comparisons test or Holm-Šídák's multiple comparisons test. p-values are noted on the graphs. The statistical tests,
492 corresponding effect sizes, and confidence intervals for each graph are in Supplementary Table 2

493 **Supplementary Figure 2: Mitochondrial dysfunction in GBA1-PD DA neurons and fibroblasts:**
494 Representative images of GBA1-E326K and GBA1-N370S fibroblasts (Ai) and DA neurons (Bi a,b) along with
495 controls, stained with TMRM to measure changes in ΔΨm (Aii a, Bii a,b) and the mitochondrial fragmentation
496 count (Aii b). Histograms representing State 3 (ATP Production) in mitochondria isolated from GBA1-E326K
497 (C a) and GBA1-N370S (C b) DA neurons and controls, as measured by Seahorse assay. Representative images
498 of western blots probed for OXPHOS complex proteins (Di) and subsequent quantification of protein expression
499 levels in GBA1 E326K (Dii a) and N370S(Dii b) DA neurons. Data represented as mean±SD; Statistics: one-
500 sample Wilcoxon rank t-test or One-way ANOVA with Kruskal-Wallis and Dunn's, Holm-Šidák or Šídák's
501 multiple comparisons test or Ordinary two-way ANOVA with Tukey's multiple comparisons test with single
502 pooled variance. p-values are noted on the graphs. The statistical tests, corresponding effect sizes, and
503 confidence intervals for each graph are in Supplementary Table 2

504 **Supplementary Figure 3: Mitophagy defects in GBA1-PD DA neurons and fibroblasts:** Representative
505 ratioed images of control and GBA1-E326K and GBA1-N370S fibroblasts (Ai) and DA neurons (Bi a,b)
506 transduced with mt-Keima plasmid and imaged imaged with excitation at 458 and 543nm and subsequent
507 quantification of the ratio ratio of signals at 543/458nm respectively (Aii, Bii a,b). Representative TEM images
508 of GBA1-E326K (Ci a) and GBA1-N370S (Ci b) DA neurons and respective isogenic controls depicting
509 autophagic vesicles and (Cii a,b) Box-and-whisker plots showing the minimum, maximum, median, and
510 interquartile range of the log(1+Y) values. Yellow Arrows indicate autolysosomes, red arrows indicate
511 autophagosomes, and green arrows indicate lysosomes in the cells. Data represented as mean±SD; Statistics:
512 One-way ANOVA with Kruskal-Wallis and Dunn's multiple comparisons test or Holm-Šidák multiple
513 comparisons test or Ordinary two-way ANOVA with Šidák multiple comparisons test. p-values are noted on the
514 graphs. The statistical tests, corresponding effect sizes, and confidence intervals for each graph are in
515 Supplementary Table 2.

516 **Supplementary Figure 4: Effect of acidic NPs and rapamycin on GBA1 – PD fibroblasts and DA neurons:**
517 Representative Confocal images (Ai) of control and mutant fibroblasts treated with Rhodamine-tagged acidic

518 NPs (Rhod-acidic NPs) and stained with Lysotracker Blue and subsequent quantification of colocalisation
519 coefficient (Aii). Representative images of control and GBA1-E326K and GBA1-N370S fibroblasts treated
520 with control and acidic NPs (Bi) and stained with the ratiometric Lysosensor Yellow/Blue DND160 subsequent
521 quantification of fluorescence ratio (Bi) to measure lysosomal pH and. C) Calibration of lysosomal pH in *GBA1*
522 mutant fibroblasts treated with and without acidic nanoparticles. Representative images of western blots and
523 quantification of GBA1 protein levels in GBA1-E326K (Di a; Dii a,b) and GBA1-N370S (Di b; Dii c,d) DA
524 neurons and respective isogenic controls treated with acidic NPs or rapamycin and probed for GBA1 and B-
525 ACTIN. GCase activity in GBA1-E326K and GBA1-N370S DA neurons and respective isogenic controls
526 treated with Acidic NPs (E a, c)/rapamycin (E b, d). Images representing rapamycin treated (Fi) and Acidic NPs
527 treated (Gi) control and GBA1-E326K and GBA1-N370S fibroblasts and stained with TMRM and subsequent
528 quantification of $\Delta\Psi m$ (Fii and Gii respectively). Histogram representing quantification of mitochondrial
529 membrane potential in *GBA1* mutant and control fibroblasts upon 3mM Diethyl succinate treatment for 30
530 minutes (H). Representative images of western blots (Ii a,b) and subsequent quantification of OXPHOS
531 complex proteins in GBA1 E326K and N370S DA neurons and respective isogenic controls treated with Acidic
532 NPs (Iii a,b) and rapamycin (Iii c,d). Representative FLIM images of ATP6V_1B2-mNeongreen in Control and
533 GBA1-PD fibroblasts co-transfected with ATP6V_0a3-mScarlet and treated with/without acidic NPs (Ji) and
534 subsequent quantification of mean lifetime (τ_m) of ATP6V_1B2 (Jii). Data represented as mean±SD; Mann-
535 Whitney's test, one-sample Wilcoxon rank t-test or Ordinary two-way ANOVA with Tukey's multiple
536 comparisons test or Uncorrected Fisher's LSD with single pooled variance. p-values are noted on the graphs.
537 The statistical tests, corresponding effect sizes, and confidence intervals for each graph are in Supplementary
538 Table 2
539

540 **Methodology:**

541 **Cell lines and ethics committee approval:**

542 The human iPSC (hiPSC) and fibroblast lines used in the study, along with their sources, are detailed in Table 1.
543 Fibroblasts were cultured in DMEM (1X) + GlutaMAX™ basal media (Gibco 2206106), 10% (v/v) Foetal Bovine
544 Serum (Gibco 10270098), and 1% antibiotic-antimycotic (Gibco 15240096), and incubated at 37 ºC with 5% CO_2.
545 The media was changed every 72 hours, and the cells were passaged upon reaching 80% confluency using 0.25%
546 Trypsin-EDTA (Gibco 25200056). Passages between 9 and 15 were used for experimental purposes. Human
547 GBA1 patient-derived iPSC lines were cultured under feeder-free conditions on Geltrex-coated 6-well plates,
548 using mTeSR Plus medium and were passaged every 4-5 days with a 0.5 mM EDTA solution or upon reaching
549 80% confluency. Passage numbers between 20 and 30 were employed for differentiation purposes.

550 **Human pluripotent stem cell-derived DA neurons**

551 DA neurons were generated from iPSCs using a step-by-step differentiation protocol, as previously described[74].
552 Briefly, 90-95% confluent hiPSCs were cultured on Geltrex-coated plates and maintained in N2B27 medium,
553 which is a 1:1 mix of Neurobasal (Gibco, 21103049) supplemented with 1X B27 (Gibco, 17504044), Glutamax
554 (Gibco, 35050-038), and 0.5X Anti-anti (Gibco, 15240096), and DMEM-F12 (Gibco, 10565018) supplemented
555 with 1X N2 supplement (Gibco, 17502048), 1X MEM Non-Essential Amino Acids (Gibco, 11140-050), 0.5X
556 Anti-anti (Gibco, 15420096), 50 μM β-mercaptoethanol (Gibco, 21985-023), and human Insulin Solution (Sigma,
557 I9278). Daily media changes were conducted for the first 14 days. On day 0, the media was supplemented with
558 5 μM SB431542 (Tocris Bioscience, 1614/10), 2 μM Dorsomorphin (Tocris Bioscience, 3093/10), and 1 μM
559 CHIR99021 until day 2. From day 2 to day 7, 1 μM Purmorphamine (Merck Millipore, SML0868) was added to
560 the mix. From day 8 to day 14, CHIR99021 and SB431542 were removed from the medium, and the cells were
561 maintained with Dorsomorphin and Purmorphamine in N2B27. Cells were dissociated with 1 mg/mL Dispase
562 (Gibco, 17105041) on days 4 and 14. After patterning for 14 days, the midbrain DA neuronal precursor cells
563 (NPCs) were maintained in N2B27 medium until day 18. On day 19, the cells were dissociated with Accutase
564 (Gibco, A1110501) and plated onto Geltrex-coated plates at a density of 2 × 10^5 cells/cm² and terminally
565 differentiated with N2B27 medium supplemented with Compound E (Enzo Lifesciences, ALX-270-415-C250)
566 and 10 μM Rho-kinase inhibitor, Y-27632 dihydrochloride (Tocris, 1254) from day 20 until day 70-75, with media
567 changes twice a week. DA neurons between days 70 and 75 were used for downstream experiments.

568 **Nanoparticle, rapamycin and diethyl succinate treatment**

569 Control and acidic NPs, composed of poly(ethylene-succinate) and poly(ethylene tetrafluorosuccinate-co-
570 succinate) respectively, were obtained from Prof. Mark Grinstaff and Prof. Orian Shirihai. The synthesis of the
571 nanoparticles is described in [31]. The nanoparticles were stored at -80°C in aliquots and thawed fresh prior to
572 treatment. Aliquots of 75 mg/mL nanoparticles were thawed to room temperature, vortexed thoroughly, and added
573 to the cells at a concentration of 180 µg/mL in fresh culture medium for 12-16 hours before the experiment. A
574 stock solution of 200 µM rapamycin (Sigma, R0395) was prepared in DMSO and sterile filtered before being
575 stored as aliquots at -20ºC. This stock solution was diluted to 200 nM in medium before being added to the cells.
576 The cells were treated with 200 nM rapamycin for 12-16 hours before proceeding with the experiments unless
577 mentioned otherwise. Diethyl Succinate (Merck, 112402) was diluted to 3 mM in culture media and sterile-filtered
578 and added onto cells 30 minutes prior to measuring the ΔΨm using TMRM.

579 **Generation of lentivirus and transduction:**

580 pLV-Ef1a-3xHA-ATP6V1B2-mNeonGreen and pLV-Ef1a-3xFlag-ATP6Voa3-mScarlet plasmids were kindly
581 provided by Dr. Wilhelm Palm (EPR 462 and EPR 475, European Plasmid Repository). pHAGE-mt-mKeima
582 was a generous gift from Prof. Richard Youle (131626, Addgene). Lentiviral plasmids were packaged using
583 psPAX2 and pMD2.G in HEK293T cells with Xtremegene-HP transfection reagent (Merck, 6366236001),
584 according to the manufacturer's instructions. The media supernatant containing viruses was collected 48 and 72
585 hours post-transfection and concentrated using Lenti-X transfection reagent (Takara, 631231) with overnight
586 incubation, followed by centrifugation at 2000 rpm for 1 hour at 4ºC. The pellet was then resuspended in DMEM-
587 F12 medium and stored at -80ºC for further use. 72-96 hours prior to imaging, fibroblasts or DA neurons were
588 treated with lentiviral particles. 24 hours post-treatment, the media was replaced with regular culture medium
589 and incubated for another 48 hours before imaging.

590 **Confocal imaging**

591 DMEM-F12 medium (Gibco, 21041025) or BrainPhys medium (Stem Cell Technologies, 05796) served as a
592 recording buffer for live cell imaging of fibroblasts and DA neurons. All images were acquired using a Carl Zeiss
593 LSM 880 Confocal Laser Scanning microscope with Zen Black Software and a 63×/1.40 oil immersion lens at
594 37°C. Fixed and stained fibroblasts were also imaged with the same equipment.

595 **Lysosensor Yellow/Blue DND 160**

596 The cells were washed with DPBS and incubated for 4 minutes in the recording buffer containing 3 µM
597 Lysosensor Yellow/Blue DND 160 (Invitrogen, L7545) at 37°C. After incubation, the dye was washed twice with

PBS and imaged in fresh recording buffer using the UV laser at 355 nm. The dual emission maxima of the dye (440 nm/540 nm) were detected using spectral scanning (lambda scan mode) on the Zeiss LSM 880. Images were subsequently linearly unmixed employing the ZEN Black software to separate the 440 nm and 540 nm emission images. The ratio of 440/540 nm was then calculated using the Ratio Plus plugin on ImageJ/Fiji software to determine the lysosomal acidity of fibroblasts and DA neurons

Lysosomal pH measurement

The lysosomal pH was measured using Lysosensor Yellow/Blue DND-160 (L7545, Invitrogen). Fibroblasts cultured on fluorodishes were treated with pH calibration buffer containing Monensin (Sigma, M5273) and Nigericin (Sigma, N7143), with a pH ranging from 3.5 to 7.0 and stained with Lysosensor Yellow/Blue DND 160. The cells were incubated with 2 µM for 5 minutes at room temperature (RT) and imaged as previously mentioned. The 440/540 fluorescence ratio was measured for each calibration buffer. A lysosomal pH calibration curve was established by correlating the 440/540 nm ratio with the corresponding pH values using ImageJ/Fiji software.

Measurement of lysosomal proteolytic activity by DQ Red BSA

The DQ-Red BSA trafficking assay dye (Invitrogen, D12051) was utilised to examine lysosomal proteolytic activity. DA neurons were washed with DPBS, and pre-warmed medium containing DQ-Red BSA was added to the fluorodishes. The dishes were incubated at 37°C for three hours. Following the incubation period, the cells were washed with DPBS and replaced with the recording buffer prior to imaging. Cells stained with DQ-Red BSA were excited using a 561 nm Argon laser, and the emitted fluorescence was collected within the 564–740 nm range. The fluorescence intensity was quantified per cell using ImageJ/Fiji software with consistent threshold settings across all samples.

Measurement of ΔΨm using TMRM

Fibroblast or DA neurons were washed with DPBS and incubated in recording buffer containing 20 nM TMRM (Thermofisher Scientific, T668) at 37°C for 30 minutes. Following incubation, fresh recording buffer containing 20 nM TMRM was added before proceeding with imaging. The cells were excited for TMRM fluorescence at 561 nm, and images were acquired as Z-stacks. Maximum intensity projection images were then utilised to quantify the fluorescence intensity using ImageJ/Fiji software with consistent threshold settings across all samples. The TMRM images were also used to analyse the mitochondrial morphology [75].

Measurement of Lipofuscin levels

626 Lipofuscins are excited at 355 nm and fluoresce across a range from 480 to 700 nm[20]. Fibroblasts were washed
627 with the recording buffer and imaged using UV illumination at 355 nm, with images obtained through spectral
628 scanning. The images were subsequently linearly unmixed using ZEN Black software to separate the 460 nm and
629 480 nm emission images, thus distinguishing NAD(P)H from lipofuscins. The spectrally unmixed images at 480
630 nm were then utilised to calculate lipofuscin density per cell using ImageJ/Fiji software.

631 **Colocalisation of the Rhodamine-B labelled acidic NPs with the lysosomes**

632 Rhodamine B-labelled acidic NPs were treated for 12-16 hours prior to imaging the fibroblasts. On the imaging
633 day, cells were washed with the recording buffer and incubated with 50 nM LysoTracker Blue DND-22 dye
634 (Invitrogen, L7525) for 2 hours at 37°C. Following the incubation, the cells were washed with the recording
635 buffer and imaged in fresh buffer. Images were acquired using sequential excitation (405 nm for LysoTracker
636 Blue and 561 nm for Rhodamine) and emission ranges set to 420–480 nm and 570–620 nm, respectively.
637 Colocalisation Pearson's coefficient was quantified using ImageJ/Fiji software with consistent threshold settings
638 across all samples.

639 **Measurement of mitophagy using mt-Keima reporter**

640 Measurement of mitophagy was performed as previously described[76]. Untreated fibroblasts and DA neurons
641 were tranduced with lentiviral mt-Keima particles 72 hrs prior to imaging. 12-16 hours before imaging, the cells
642 were treated with acidic NPs or rapamycin. The cells were imaged using two sequential excitation wavelengths
643 (458 nm for green fluorescence and 561 nm for red fluorescence) with an emission range of 570–695 nm. The
644 laser power was set at the minimum output to allow the clear visualisation of the mt-Keima signal. The ratio of
645 the high F_{543}:F_{458} ratio values were generated using the Ratio Plus plugin in ImageJ/Fiji and was used as an index
646 of mitophagy.

647 **Fluorescence lifetime imaging microscopy (FLIM) quantification of ATP6V$_1$B2-mNeonGreen**

648 Fluorescence lifetime imaging was conducted using single-photon excitation on a multimodal time-resolved
649 fluorescence microscope as previously described[77]. This setup encompassed an 80 MHz, near-infrared,
650 femtosecond excitation source (Insight X3, Spectra Physics, Crewe, UK), a second harmonic generation unit
651 (Harmonixx SHG, APE, Berlin, Germany), a laser scanning unit (DCS-120, Becker & Hickl, Berlin, Germany),
652 an inverted microscope (Axio Observer 7, Zeiss, Cambridge, UK) featuring a high numerical aperture objective
653 (Plan-Apochromat 63x/1.4 Oil M27, Zeiss, Cambridge, UK), an ultrafast hybrid detector (HPM-100-07, Becker
654 & Hickl, Berlin, Germany), and time-correlated single photon counting (TCSPC) electronics (SPC-180NX, Becker

655 & Hickl, Berlin, Germany). Images were acquired using 473 nm excitation to minimise the ratio of acceptor to
656 donor excitation, along with 500–540 nm emission filtering to isolate fluorescence from the mNeonGreen donor.
657 Photon counts were acquired for two minutes and histogrammed at 14.6ps intervals. Curve fitting analysis was
658 performed in SPCImage (Becker & Hickl, Berlin, Germany).

659 **Lysosomal enrichment assay**

660 A lysosomal enrichment assay was conducted using the Lysosome Enrichment Kit for Tissues and Cultured Cells
661 (Thermo Scientific, 89839) according to the manufacturer's instructions. Briefly, the DA neurons were pelleted
662 and lysed with lysosome enrichment reagent A, which contained 1X protease and phosphatase inhibitors. The
663 solution was then sonicated on ice, applying 12 bursts at 9W of power (Thermo Scientific) and mixed with
664 lysosome enrichment reagent B. The solution was subsequently centrifuged at 500g for 10 minutes. 200 µL of
665 supernatant was then aliquoted for use as cell supernatant for western blotting. Lysosomes were isolated from the
666 remaining solution through gradient centrifugation. The protein concentrations of the lysosomes and cell
667 supernatant were then quantified using a BCA assay and proceeded for western blotting as discussed below.

668 **SDS-PAGE and immunoblotting**

669 Fibroblasts and DA neurons were washed with ice-cold PBS, followed by the addition of 150 µl of ice-cold RIPA
670 lysis buffer (Sigma-Aldrich, R0278), which was supplemented with protease inhibitors (Roche 4693116001),
671 PMSF (Sigma, 93482), and phosphatase inhibitors (Roche 4906837001). Cells were scraped using a plastic
672 scraper, and the lysates were transferred to 1.5 ml tubes. The lysates were rotated at 4°C for 30 minutes and
673 sonicated (3 cycles, 3 seconds each at 40% amplitude, with 5-minute intervals). Samples were centrifuged at
674 16,000 g for 30 minutes at 4°C, and the supernatant was collected. Protein concentration was determined using a
675 BCA assay kit (Thermo Scientific, 23227). A total of 20-30 µg of protein was diluted with RIPA buffer and mixed
676 with NuPAGE 4X sample buffer (Invitrogen, NP0007). The samples were heated at 95°C for 5 minutes (for
677 OXPHOS proteins, the lysates were heated at 45ºC for 5 minutes). Proteins were separated on 4–12% NuPAGE
678 Bis-Tris polyacrylamide gels (Invitrogen, NP0335) immersed in MOPS running buffer (Invitrogen, NP0001).
679 Proteins were transferred to PVDF membranes (Millipore, IPFL00010) activated in methanol using a wet transfer
680 system. Membranes were blocked in Superblock blocking buffer (Invitrogen, 37545) for 1 hour at room
681 temperature. The blots were cut where necessary before incubating with primary antibodies, which were diluted
682 in 1X blocking buffer, and incubated with the membranes overnight at 4°C. After three 10-minute washes in
683 TBST, the membranes were incubated with secondary antibodies (Li-COR Biosciences; 1:10000; IRDye® 680RD

684 Goat anti-Mouse IgG, 926-68070; IRDye® 800CW Goat anti-Rabbit IgG, 926-32211) diluted in 1% BSA/TBST
685 for 1 hour at room temperature. The membranes were washed three additional times with TBST. Fluorescent
686 signals were developed using a LiCOR Odyssey CLx system. The details of the antibodies are listed in Table 2.

687 **Immunostaining**

688 Fibroblasts were grown on coverslips, treated, and fixed with 4% (w/v) paraformaldehyde. After fixation, the
689 cells were permeabilised with 50 µg/ml digitonin in PBS for 10 minutes. The cells were then washed, blocked
690 with 3% BSA, and incubated with the following primary antibodies: citrate synthase, LAMP1, and LC3 in 3%
691 BSA for 1 hour at room temperature, followed by incubation with Alexa Fluor 488/594/647-conjugated
692 secondary antibodies for 1 hour at room temperature. Coverslips were mounted on glass slides, and images were
693 acquired using appropriate excitation and emission filters to capture fluorescent signals. Colocalisation Pearson's
694 coefficient (Mito vs LC3 and Mito vs LAMP1), lysosomal number (LAMP1 particles/cell), and autophagosome
695 number (LC3 particles/cell) were quantified using ImageJ/Fiji with consistent threshold settings across all
696 samples. The catalogue number and dilution range of the antibodies are listed in Table 2.

697 **Mitochondrial isolation**

698 Mitochondria were isolated according to the method described earlier [78] and modified for the neuronal cultures.
699 Briefly, DA neuron cell pellets were resuspended in mitochondria isolation buffer (MIB1: 225 mM Mannitol, 75
700 mM Sucrose, 5 mM HEPES, 1 mM EGTA and 1 mg/ml fatty acid free BSA) and homogenised using a ice-cold
701 Dounce tissue grinder tube (appropriate for 1-1.5 ml homogenisation volume). The homogenate was centrifuged,
702 and the mitochondrial pellet was washed and pellet down in MIB without BSA (MIB2) according to the protocol.
703 The final pellet was resuspended in a very small volume of MIB2, and the protein concentration was determined
704 using BCA Protein assay kit (Thermofisher Scientific, 23227) according to the manufacturer's specifications.The
705 isolated mitochondria were then used for respiratory measurements.

706 **Measurement of oxygen consumption rate**

707 Measurements of mitochondrial respiration were conducted with the Seahorse Bioscience XFe96 bioanalyzer
708 using the Seahorse XF Cell Mito Stress Test Kit (Agilent #103015-100). Final maturation of iPSCs into DA
709 neurons were performed in XF96 cell culture microplates (Agilent #102416-100). On the day of the experiment,
710 the culture medium was replaced with Seahorse XF Base medium (Agilent #103334-100) supplemented with
711 1 mM pyruvate (Gibco #11360070), 2 mM glutamine (Gibco #25030081) and 10 mM glucose (Gibco #A2494001)

712 and incubated for 30 min at 37 °C in a CO_2-free incubator before loading into the Seahorse Analyser. After
713 measuring basal respiration, the drugs oligomycin (5 μM), FCCP (1.5 μM), and rotenone/antimycin A
714 (0.5 μM/0.5 μM) were added to each well in sequential order. After the assay, cells were stained with Hoechst
715 33342 (5 μM; Thermo Scientific #62249) for 30 min. ImageXpress was then used to count the number of cell
716 nuclei (cell numbers) in each well and normalised to get the basal respiration rate values.
717 The respiratory measurements of isolated mitochondria from mixed neuronal cultures were performed using a
718 modified method described earlier[79] for Seahorse XFe96 cell culture plates assay. Briefly, 5 or 10 μg of
719 mitochondrial protein was resuspended in 30 μL (1 well) of individual substrate mix (for example, pyruvate/malate
720 substrate + mitochondria assay solution - MAS) and plated into each well. The cell culture plate was centrifuged
721 at 2,000g for 20 minutes at 4 °C to form a uniform layer of mitochondria at the bottom. After centrifugation, 150
722 μL of substrate solution was carefully added to each well. Fresh injection solutions were made in MAS without
723 BSA and loaded into the cartridge, and calibrated according to the manufacturer's specifications. After calibration,
724 the culture plate with mitochondria was inserted, and the assay was run essentially as described in the method.

725 **Transmission electron microscopy (TEM)**

726 TEM was performed as previously described [76]. Briefly, fibroblasts and DA neurons grown on coverslips were
727 fixed in electron microscopy (EM) fixative containing 2% glutaraldehyde (EMS, 16365) and 2%
728 paraformaldehyde (EMS, 15710) in 0.1 M sodium cacodylate for 1 hour. Following fixation, cells were washed
729 with 0.1 M cacodylate buffer (EMS, 11650) and then fixed in a solution of 1% osmium tetroxide (EMS, 19150)
730 and 1% potassium ferricyanide (EMS, 25120-20) in 0.1 M sodium cacodylate. This was followed by sequential
731 dehydration using ethanol. Coverslips were then embedded in epoxy resin (Araldite Kit, Agar Scientific Ltd.,
732 CY212) according to standard protocols. The embedded samples were sectioned into 50 nm slices using an
733 ultramicrotome equipped with a diamond knife and mounted onto copper TEM grids. The grids were stained with
734 lead citrate for 3 minutes before imaging. Images were captured using a Jeol 1400 Transmission Electron
735 Microscope at magnifications ranging from 800× to 1200× (digital magnification). Images were imported into
736 ImageJ/Fiji to quantify mitochondrial area, mitochondrial cristae density and mitochondrial aspect ratio. The
737 autophagic vesicles were classified as autophagosomes, autolysosomes and lysosomes as per [24]. Briefly, in Fig
738 3D and Fig S3C, autophagosomes typically display clear double membranes or a single membrane, darker than
739 the surrounding tissue in TEM images, with more circular shapes inside, indicating cargo (red arrows). Lysosomal
740 membranes show highly organised inner folds, while lysosomal enzymes are characterised by a darker, more
741 uniform appearance (green arrows). Autolysosomes are intermediate structures larger than lysosomes, frequently

containing intact autophagosome contents (yellow arrows). Distinct dark spots (black arrows) may indicate protein aggregates; further work is needed to confirm their identity. Mitochondria and autophagic vesicles were manually traced to measure their areas, and the structures were verified by an Electron Microscopy expert. Quantification was performed in a double-blind manner.

Quantification and statistical analysis

All statistical analyses were performed using GraphPad Prism (version10; GraphPad Software) and verified by a qualified statistician. Sample sizes (n) for each experiment represent values from at least 3 independent experiments.

For comparisons between two datasets, paired t-test or two-tailed unpaired t-tests were used for normally distributed data; when normality was not met, the Mann–Whitney test was used. For multi-group comparisons, one-way ANOVA was performed, followed by the Kruskal–Wallis test, with Dunn's multiple comparisons correction applied. For experiments involving independent comparisons within the group, ordinary two-way ANOVA with Tukey's multiple comparisons test (single pooled variance), Šidák multiple comparisons or Uncorrected Fisher's LSD (single pooled variance) was used. Samples normalised to a reference value of 1 were analysed using one-sample Wilcoxon rank t-tests (Supplementary table 2).

Where multiple comparisons were conducted, adjusted p-values are reported following the appropriate post hoc correction. Adjusted p-values are provided in the graphs. Statistical significance was defined as adjusted $p < 0.05$.

The mitochondrial morphology parameters were heavily skewed, hence the values were log(Y) transformed before calculating the effect size, confidence intervals and unpaired t-test. Autophagic vesicle counts in neurons contained zeros; therefore, values were log(1+Y) transformed prior to two-way ANOVA. Effect sizes are reported as partial eta-squared (partial η^2) with 95% confidence intervals.

Data are presented in the figures as mean ± standard deviation (SD). Effect sizes (for Mann-Whitney's test comparison - Hedges' g; Unpaired t-test – Cohen's d; one-sample t-test - Glass's Δ; ω^2 - for one-way ANOVA**;** partial η^2 - for two-way ANOVA). The noncentral F distribution method (for ANOVA) or the Bootstrap (all others) was used to compute 95% confidence intervals to aid interpretation of the magnitude and precision of observed effects. Wherever possible, individual data points and raw data distributions are shown in figures, and all raw numerical values used to generate graphs are provided in Supplementary Table 1. The statistical test, effect size,

769 and confidence interval values for each graph are included in Supplementary Table 2 to promote transparency and
770 reproducibility.

771 **Abbreviations:**

772 **GBA1** - Glucocerebrocidase

773 **PD** – Parkinson's Disease

774 **GCase** – β-glucocerebrosidase enzyme

775 **pH** – potential of Hydrogen

776 **V-ATPase** – Vascular ATPase

777 **iPSCs** – induced Pluripotent Stem Cells

778 **DA neuron** – Dopaminergic neurons

779 **OXPHOS** – Oxidative Phosphorylation

780 **ΔΨm** – Mitochondrial Membrane Potential

781 **TEM –** Transmission Electron Microscopy

782 **TMRM** - TetraMethyl-Rhodamine Methyl ester

783 **MTORC1** – Mammalian Target of Rapamycin Complex I

784 **FLIM-FRET** - Fluorescence Lifetime Imaging (FLIM) with Förster Resonance Energy Transfer

785 **NPs** - Nanoparticles

References:

1. Sidransky E, Nalls MA, Aasly JO, Aharon-Peretz J, Annesi G, Barbosa ER, et al. Multicenter Analysis of Glucocerebrosidase Mutations in Parkinson's Disease. N Engl J Med. 2009;361:1651–61. https://doi.org/10.1056/NEJMoa0901281

2. Furderer ML, Hertz E, Lopez GJ, Sidransky E. Neuropathological Features of Gaucher Disease and Gaucher Disease with Parkinsonism. IJMS. 2022;23:5842. https://doi.org/10.3390/ijms23105842

3. Lwin A. Glucocerebrosidase mutations in subjects with parkinsonism. Molecular Genetics and Metabolism. 2004;81:70–3. https://doi.org/10.1016/j.ymgme.2003.11.004

4. Duran R, Mencacci NE, Angeli AV, Shoai M, Deas E, Houlden H, et al. The glucocerobrosidase E326K variant predisposes to Parkinson's disease, but does not cause Gaucher's disease. Movement Disorders. 2013;28:232–6. https://doi.org/10.1002/mds.25248

5. Henrich MT, Oertel WH, Surmeier DJ, Geibl FF. Mitochondrial dysfunction in Parkinson's disease – a key disease hallmark with therapeutic potential. Mol Neurodegeneration. 2023;18:83. https://doi.org/10.1186/s13024-023-00676-7

6. Osellame LD, Rahim AA, Hargreaves IP, Gegg ME, Richard-Londt A, Brandner S, et al. Mitochondria and Quality Control Defects in a Mouse Model of Gaucher Disease—Links to Parkinson's Disease. Cell Metabolism. 2013;17:941–53. https://doi.org/10.1016/j.cmet.2013.04.014

7. Lawrence RE, Zoncu R. The lysosome as a cellular centre for signalling, metabolism and quality control. Nat Cell Biol. 2019;21:133–42. https://doi.org/10.1038/s41556-018-0244-7

8. Ponsford AH, Ryan TA, Raimondi A, Cocucci E, Wycislo SA, Fröhlich F, et al. Live imaging of intra-lysosome pH in cell lines and primary neuronal culture using a novel genetically encoded biosensor. Autophagy. 2021;17:1500–18. https://doi.org/10.1080/15548627.2020.1771858

9. Chin MY, Ang K-H, Davies J, Alquezar C, Garda VG, Rooney B, et al. Phenotypic Screening Using High-Content Imaging to Identify Lysosomal pH Modulators in a Neuronal Cell Model. ACS Chem Neurosci. 2022;13:1505–16. https://doi.org/10.1021/acschemneuro.1c00804

10. Dehay B, Martinez-Vicente M, Caldwell GA, Caldwell KA, Yue Z, Cookson MR, et al. Lysosomal impairment in Parkinson's disease. Movement Disorders. 2013;28:725–32. https://doi.org/10.1002/mds.25462

11. Falace A, Volpedo G, Scala M, Zara F, Striano P, Fassio A. V-ATPase Dysfunction in the Brain: Genetic Insights and Therapeutic Opportunities. Cells. 2024;13:1441. https://doi.org/10.3390/cells13171441

12. Rujano MA, Cannata Serio M, Panasyuk G, Péanne R, Reunert J, Rymen D, et al. Mutations in the X-linked *ATP6AP2* cause a glycosylation disorder with autophagic defects. Journal of Experimental Medicine. 2017;214:3707–29. https://doi.org/10.1084/jem.20170453

13. Byrns CN, Bonini NM. An Integrated Multi-omics Approach Identifies Therapeutic Potential for ATP6V1A in Late Onset Alzheimer's Disease. Neuron. 2021;109:193–4. https://doi.org/10.1016/j.neuron.2020.12.015

14. Wang M, Li A, Sekiya M, Beckmann ND, Quan X, Schrode N, et al. Transformative Network Modeling of Multi-omics Data Reveals Detailed Circuits, Key Regulators, and Potential Therapeutics for Alzheimer's Disease. Neuron. 2021;109:257-272.e14. https://doi.org/10.1016/j.neuron.2020.11.002

15. Fassio A, Esposito A, Kato M, Saitsu H, Mei D, Marini C, et al. De novo mutations of the ATP6V1A gene cause developmental encephalopathy with epilepsy. Brain. 2018;141:1703–18. https://doi.org/10.1093/brain/awy092

16. Guerrini R, Mei D, Kerti-Szigeti K, Pepe S, Koenig MK, Von Allmen G, et al. Phenotypic and genetic spectrum of ATP6V1A encephalopathy: a disorder of lysosomal homeostasis. Brain. 2022;145:2687–703. https://doi.org/10.1093/brain/awac145

17. Im E, Jiang Y, Stavrides PH, Darji S, Erdjument-Bromage H, Neubert TA, et al. Lysosomal dysfunction in Down syndrome and Alzheimer mouse models is caused by v-ATPase inhibition by Tyr^{682} -phosphorylated APP βCTF. Sci Adv. 2023;9:eadg1925. https://doi.org/10.1126/sciadv.adg1925

18. Schöndorf DC, Aureli M, McAllister FE, Hindley CJ, Mayer F, Schmid B, et al. iPSC-derived neurons from GBA1-associated Parkinson's disease patients show autophagic defects and impaired calcium homeostasis. Nat Commun. 2014;5:4028. https://doi.org/10.1038/ncomms5028

19. Settembre C, Fraldi A, Medina DL, Ballabio A. Signals from the lysosome: a control centre for cellular clearance and energy metabolism. Nat Rev Mol Cell Biol. 2013;14:283–96. https://doi.org/10.1038/nrm3565

20. Croce AC, Bottiroli G. Autofluorescence spectroscopy and imaging: a tool for biomedical research and diagnosis. Eur J Histochem [Internet]. 2014 [cited 2025 Mar 2]; https://doi.org/10.4081/ejh.2014.2461

21. Song SB, Shim W, Hwang ES. Lipofuscin Granule Accumulation Requires Autophagy Activation. Molecules and Cells. 2023;46:486–95. https://doi.org/10.14348/molcells.2023.0019

22. Haltia M, Goebel HH. The neuronal ceroid-lipofuscinoses: A historical introduction. Biochimica et Biophysica Acta (BBA) - Molecular Basis of Disease. 2013;1832:1795–800. https://doi.org/10.1016/j.bbadis.2012.08.012

23. Sun N, Malide D, Liu J, Rovira II, Combs CA, Finkel T. A fluorescence-based imaging method to measure in vitro and in vivo mitophagy using mt-Keima. Nat Protoc. 2017;12:1576–87. https://doi.org/10.1038/nprot.2017.060

24. Neikirk K, Vue Z, Katti P, Rodriguez BI, Omer S, Shao J, et al. Systematic Transmission Electron Microscopy-Based Identification and 3D Reconstruction of Cellular Degradation Machinery. Advanced Biology. 2023;7:2200221. https://doi.org/10.1002/adbi.202200221

25. Ratto E, Chowdhury SR, Siefert NS, Schneider M, Wittmann M, Helm D, et al. Direct control of lysosomal catabolic activity by mTORC1 through regulation of V-ATPase assembly. Nat Commun. 2022;13:4848. https://doi.org/10.1038/s41467-022-32515-6

26. Mauvezin C, Nagy P, Juhász G, Neufeld TP. Autophagosome–lysosome fusion is independent of V-ATPase-mediated acidification. Nat Commun. 2015;6:7007. https://doi.org/10.1038/ncomms8007

27. Suhling K, Hirvonen LM, Levitt JA, Chung P-H, Tregidgo C, Le Marois A, et al. Fluorescence lifetime imaging (FLIM): Basic concepts and some recent developments. Medical Photonics. 2015;27:3–40. https://doi.org/10.1016/j.medpho.2014.12.001

28. Bindels DS, Haarbosch L, Van Weeren L, Postma M, Wiese KE, Mastop M, et al. mScarlet: a bright monomeric red fluorescent protein for cellular imaging. Nat Methods. 2017;14:53–6. https://doi.org/10.1038/nmeth.4074

29. Blacker TS, Chen W, Avezov E, Marsh RJ, Duchen MR, Kaminski CF, et al. Investigating State Restriction in Fluorescent Protein FRET Using Time-Resolved Fluorescence and Anisotropy. J Phys Chem C. 2017;121:1507–14. https://doi.org/10.1021/acs.jpcc.6b11235

30. Masters TA, Marsh RJ, Armoogum DA, Nicolaou N, Larijani B, Bain AJ. Restricted State Selection in Fluorescent Protein Förster Resonance Energy Transfer. J Am Chem Soc. 2013;135:7883–90. https://doi.org/10.1021/ja312230b

31. Zeng J, Acin-Perez R, Assali EA, Martin A, Brownstein AJ, Petcherski A, et al. Restoration of lysosomal acidification rescues autophagy and metabolic dysfunction in non-alcoholic fatty liver disease. Nat Commun. 2023;14:2573. https://doi.org/10.1038/s41467-023-38165-6

32. Zhang J, Zeng W, Han Y, Lee W-R, Liou J, Jiang Y. Lysosomal LAMP proteins regulate lysosomal pH by direct inhibition of the TMEM175 channel. Molecular Cell. 2023;83:2524-2539.e7. https://doi.org/10.1016/j.molcel.2023.06.004

33. Bae E-J, Yang NY, Lee C, Lee H-J, Kim S, Sardi SP, et al. Loss of glucocerebrosidase 1 activity causes lysosomal dysfunction and α-synuclein aggregation. Exp Mol Med. 2015;47:e153–e153. https://doi.org/10.1038/emm.2014.128

34. Burbulla LF, Jeon S, Zheng J, Song P, Silverman RB, Krainc D. A modulator of wild-type glucocerebrosidase improves pathogenic phenotypes in dopaminergic neuronal models of Parkinson's disease. Sci Transl Med. 2019;11:eaau6870. https://doi.org/10.1126/scitranslmed.aau6870

35. García-Sanz P, Orgaz L, Bueno-Gil G, Espadas I, Rodríguez-Traver E, Kulisevsky J, et al. N370S -*GBA1* mutation causes lysosomal cholesterol accumulation in Parkinson's disease. Movement Disorders. 2017;32:1409–22. https://doi.org/10.1002/mds.27119

36. Kilpatrick BS, Magalhaes J, Beavan MS, McNeill A, Gegg ME, Cleeter MWJ, et al. Endoplasmic reticulum and lysosomal Ca2+ stores are remodelled in GBA1-linked Parkinson disease patient fibroblasts. Cell Calcium. 2016;59:12–20. https://doi.org/10.1016/j.ceca.2015.11.002

37. Magalhaes J, Gegg ME, Migdalska-Richards A, Doherty MK, Whitfield PD, Schapira AHV. Autophagic lysosome reformation dysfunction in glucocerebrosidase deficient cells: relevance to Parkinson disease. Hum Mol Genet. 2016;25:3432–45. https://doi.org/10.1093/hmg/ddw185

38. Navarro-Romero A, Fernandez-Gonzalez I, Riera J, Montpeyo M, Albert-Bayo M, Lopez-Royo T, et al. Lysosomal lipid alterations caused by glucocerebrosidase deficiency promote lysosomal dysfunction, chaperone-mediated-autophagy deficiency, and alpha-synuclein pathology. npj Parkinsons Dis. 2022;8:126. https://doi.org/10.1038/s41531-022-00397-6

39. Pitcairn C, Wani WY, Mazzulli JR. Dysregulation of the autophagic-lysosomal pathway in Gaucher and Parkinson's disease. Neurobiology of Disease. 2019;122:72–82. https://doi.org/10.1016/j.nbd.2018.03.008

40. Baden P, Perez MJ, Raji H, Bertoli F, Kalb S, Illescas M, et al. Glucocerebrosidase is imported into mitochondria and preserves complex I integrity and energy metabolism. Nat Commun. 2023;14:1930. https://doi.org/10.1038/s41467-023-37454-4

41. Gegg ME, Schapira AHV. Mitochondrial dysfunction associated with glucocerebrosidase deficiency. Neurobiology of Disease. 2016;90:43–50. https://doi.org/10.1016/j.nbd.2015.09.006

42. Kim S, Wong YC, Gao F, Krainc D. Dysregulation of mitochondria-lysosome contacts by GBA1 dysfunction in dopaminergic neuronal models of Parkinson's disease. Nat Commun. 2021;12:1807. https://doi.org/10.1038/s41467-021-22113-3

43. Rubilar JC, Outeiro TF, Klein AD. The lysosomal β-glucocerebrosidase strikes mitochondria: implications for Parkinson's therapeutics. Brain. 2024;147:2610–20. https://doi.org/10.1093/brain/awae070

44. Li H, Ham A, Ma TC, Kuo S-H, Kanter E, Kim D, et al. Mitochondrial dysfunction and mitophagy defect triggered by heterozygous *GBA* mutations. Autophagy. 2019;15:113–30. https://doi.org/10.1080/15548627.2018.1509818

45. Miyazono Y, Hirashima S, Ishihara N, Kusukawa J, Nakamura K, Ohta K. Uncoupled mitochondria quickly shorten along their long axis to form indented spheroids, instead of rings, in a fission-independent manner. Sci Rep. 2018;8:350. https://doi.org/10.1038/s41598-017-18582-6

46. Zong Y, Li H, Liao P, Chen L, Pan Y, Zheng Y, et al. Mitochondrial dysfunction: mechanisms and advances in therapy. Sig Transduct Target Ther. 2024;9:124. https://doi.org/10.1038/s41392-024-01839-8

47. Shinde S, Pasupathy K. Respiratory-chain enzyme activities in isolated mitochondria of lymphocytes from patients with *Parkinson's disease* : Preliminary study. Neurol India. 2006;54:390. https://doi.org/10.4103/0028-3886.28112

48. Haas RH, Nasirian F, Nakano K, Ward D, Pay M, Hill R, et al. Low platelet mitochondrial complex I and complex II/III activity in early untreated parkinson's disease. Annals of Neurology. 1995;37:714–22. https://doi.org/10.1002/ana.410370604

49. Tintos-Hernández JA, Santana A, Keller KN, Ortiz-González XR. Lysosomal dysfunction impairs mitochondrial quality control and is associated with neurodegeneration in *TBCK* encephaloneuronopathy. Brain Communications. 2021;3:fcab215. https://doi.org/10.1093/braincomms/fcab215

50. Song Q, Meng B, Xu H, Mao Z. The emerging roles of vacuolar-type ATPase-dependent Lysosomal acidification in neurodegenerative diseases. Transl Neurodegener. 2020;9:17. https://doi.org/10.1186/s40035-020-00196-0

51. Lipton JO, Sahin M. The Neurology of mTOR. Neuron. 2014;84:275–91. https://doi.org/10.1016/j.neuron.2014.09.034

52. Yates SC, Zafar A, Hubbard P, Nagy S, Durant S, Bicknell R, et al. Dysfunction of the mTOR pathway is a risk factor for Alzheimer's disease. acta neuropathol commun. 2013;1:3. https://doi.org/10.1186/2051-5960-1-3

53. Chen L, Saito R, Noda-Narita S, Kassai H, Aiba A. Hyperactive mTORC1 in striatum dysregulates dopamine receptor expression and odor preference behavior. Front Neurosci. 2024;18:1461178. https://doi.org/10.3389/fnins.2024.1461178

54. Liu X, Li Y, Yu L, Vickstrom CR, Liu Q. VTA mTOR Signaling Regulates Dopamine Dynamics, Cocaine-Induced Synaptic Alterations, and Reward. Neuropsychopharmacol. 2018;43:1066–77. https://doi.org/10.1038/npp.2017.247

55. Liu Z, Zhuang W, Cai M, Lv E, Wang Y, Wu Z, et al. Kaemperfol Protects Dopaminergic Neurons by Promoting mTOR-Mediated Autophagy in Parkinson's Disease Models. Neurochem Res [Internet]. 2022 [cited 2025 Feb 26]; https://doi.org/10.1007/s11064-022-03819-2

56. Ebner M, Fröhlich F, Haucke V. Mechanisms and functions of lysosomal lipid homeostasis. Cell Chemical Biology. 2025;32:392–407. https://doi.org/10.1016/j.chembiol.2025.02.003

57. Hosios AM, Wilkinson ME, McNamara MC, Kalafut KC, Torrence ME, Asara JM, et al. mTORC1 regulates a lysosome-dependent adaptive shift in intracellular lipid species. Nat Metab. 2022;4:1792–811. https://doi.org/10.1038/s42255-022-00706-6

58. Sillence DJ. Glucosylceramide modulates endolysosomal pH in Gaucher disease. Molecular Genetics and Metabolism. 2013;109:194–200. https://doi.org/10.1016/j.ymgme.2013.03.015

59. Coffey EE, Beckel JM, Laties AM, Mitchell CH. Lysosomal alkalization and dysfunction in human fibroblasts with the Alzheimer's disease-linked presenilin 1 A246E mutation can be reversed with cAMP. Neuroscience. 2014;263:111–24. https://doi.org/10.1016/j.neuroscience.2014.01.001

60. Kim S-H, Cho Y-S, Kim Y, Park J, Yoo S-M, Gwak J, et al. Endolysosomal impairment by binding of amyloid beta or MAPT/Tau to V-ATPase and rescue via the HYAL-CD44 axis in Alzheimer disease. Autophagy. 2023;19:2318–37. https://doi.org/10.1080/15548627.2023.2181614

61. Bourdenx M, Daniel J, Genin E, Soria FN, Blanchard-Desce M, Bezard E, et al. Nanoparticles restore lysosomal acidification defects: Implications for Parkinson and other lysosomal-related diseases. Autophagy. 2016;12:472–83. https://doi.org/10.1080/15548627.2015.1136769

62. Sabers CJ, Martin MM, Brunn GJ, Williams JM, Dumont FJ, Wiederrecht G, et al. Isolation of a Protein Target of the FKBP12-Rapamycin Complex in Mammalian Cells. Journal of Biological Chemistry. 1995;270:815–22. https://doi.org/10.1074/jbc.270.2.815

63. Capristo M, Del Dotto V, Tropeano CV, Fiorini C, Caporali L, La Morgia C, et al. Rapamycin rescues mitochondrial dysfunction in cells carrying the m.8344A > G mutation in the mitochondrial tRNALys. Mol Med. 2022;28:90. https://doi.org/10.1186/s10020-022-00519-z

64. Zheng W, Li K, Zhong M, Wu K, Zhou L, Huang J, et al. Mitophagy activation by rapamycin enhances mitochondrial function and cognition in 5×FAD mice. Behavioural Brain Research. 2024;463:114889. https://doi.org/10.1016/j.bbr.2024.114889

65. De La Cruz López KG, Toledo Guzmán ME, Sánchez EO, García Carrancá A. mTORC1 as a Regulator of Mitochondrial Functions and a Therapeutic Target in Cancer. Front Oncol. 2019;9:1373. https://doi.org/10.3389/fonc.2019.01373

66. Morita M, Gravel S-P, Hulea L, Larsson O, Pollak M, St-Pierre J, et al. mTOR coordinates protein synthesis, mitochondrial activity and proliferation. Cell Cycle. 2015;14:473–80. https://doi.org/10.4161/15384101.2014.991572

67. Carmona-Gutierrez D, Hughes AL, Madeo F, Ruckenstuhl C. The crucial impact of lysosomes in aging and longevity. Ageing Research Reviews. 2016;32:2–12. https://doi.org/10.1016/j.arr.2016.04.009

68. Pietrafesa D, Casamassa A, Benassi B, Santoro M, Marano M, Consales C, et al. Investigating the Impact of the Parkinson's-Associated GBA1 E326K Mutation on β-Glucocerebrosidase Dimerization and Interactome Dynamics Through an In Silico Approach. IJMS. 2024;25:11443. https://doi.org/10.3390/ijms252111443

69. Steet RA, Chung S, Wustman B, Powe A, Do H, Kornfeld SA. The iminosugar isofagomine increases the activity of N370S mutant acid β-glucosidase in Gaucher fibroblasts by several mechanisms. Proc Natl Acad Sci USA. 2006;103:13813–8. https://doi.org/10.1073/pnas.0605928103

70. Wei RR, Hughes H, Boucher S, Bird JJ, Guziewicz N, Van Patten SM, et al. X-ray and Biochemical Analysis of N370S Mutant Human Acid β-Glucosidase. Journal of Biological Chemistry. 2011;286:299–308. https://doi.org/10.1074/jbc.M110.150433

71. Matassini C, Warren J, Wang B, Goti A, Cardona F, Morrone A, et al. Imino- and Azasugar Protonation Inside Human Acid β-Glucosidase, the Enzyme that is Defective in Gaucher Disease. Angew Chem Int Ed. 2020;59:10466–9. https://doi.org/10.1002/anie.202002850

72. Salvioli R, Tatti M, Scarpa S, Moavero SM, Ciaffoni F, Felicetti F, et al. The N370S (Asn370→Ser) mutation affects the capacity of glucosylceramidase to interact with anionic phospholipid-containing membranes and saposin C. Biochemical Journal. 2005;390:95–103. https://doi.org/10.1042/BJ20050325

73. Offman MN, Krol M, Silman I, Sussman JL, Futerman AH. Molecular Basis of Reduced Glucosylceramidase Activity in the Most Common Gaucher Disease Mutant, N370S. Journal of Biological Chemistry. 2010;285:42105–14. https://doi.org/10.1074/jbc.M110.172098

74. Virdi GS, Choi ML, Evans JR, Yao Z, Athauda D, Strohbuecker S, et al. Protein aggregation and calcium dysregulation are hallmarks of familial Parkinson's disease in midbrain dopaminergic neurons. npj Parkinsons Dis. 2022;8:162. https://doi.org/10.1038/s41531-022-00423-7

75. Merrill RA, Flippo KH, Strack S. Measuring Mitochondrial Shape with ImageJ. In: Strack S, Usachev YM, editors. Techniques to Investigate Mitochondrial Function in Neurons [Internet]. New York, NY: Springer New York; 2017 [cited 2025 Apr 10]. p. 31–48. https://doi.org/10.1007/978-1-4939-6890-9_2

76. Chung C-Y, Singh K, Sheshadri P, Valdebenito GE, Chacko AR, Costa Besada MA, et al. Inhibition of the PI3K-AKT-MTORC1 axis reduces the burden of the m.3243A>G mtDNA mutation by promoting mitophagy and improving mitochondrial function. Autophagy. 2024;1–16. https://doi.org/10.1080/15548627.2024.2437908

77. Félix SS, O'Toole P, Oliveira NAS, Pinho BR, Blacker TS, Fernandes F, et al. Pathological mutation in SMN impairs modulation of GAR1 phase separation linking condensate dysfunction to Spinal Muscular Atrophy [Internet]. Biochemistry; 2025 [cited 2025 Mar 3]. https://doi.org/10.1101/2025.01.30.635772

78. Singh K, Duchen MR. Analysis of Organization and Activity of Mitochondrial Respiratory Chain Complexes in Primary Fibroblasts Using Blue Native PAGE. Methods Mol Biol. 2022;2497:339–48. https://doi.org/10.1007/978-1-0716-2309-1_25

79. Boutagy NE, Rogers GW, Pyne ES, Ali MM, Hulver MW, Frisard MI. Using Isolated Mitochondria from Minimal Quantities of Mouse Skeletal Muscle for High throughput Microplate Respiratory Measurements. J Vis Exp. 2015;e53216. https://doi.org/10.3791/53216

Declarations

Ethics approval

The source and ethical approval committee for the iPSCs used in the study is tabulated in table 1.

Consent for publication

Not applicable

Availability of data and materials

All data generated or analysed during this study are included in this published article and its supplementary information files.

Competing interests

The authors declared no competing interests in this research.

Funding

This project was funded by the Michael J Fox Foundation (Project number E27234 to MRD) and the Parkinson's UK Foundation (G-2103 to MRD and PS).

Authors' contributions

P.S., M.R.D - Conceptualisation, funding acquisition, investigation, visualization, methodology, writing–original draft, project administration, writing–review and editing. A.C.B –methodology, investigation, visualisation and data analysis. S.K, A.F, I.K, K.S and T.S.B– Methodology, investigation and data analysis. O.S, J.Z and M.G – Resources.

Corresponding authors

Michael Duchen (m.duchen@ucl.ac.uk) and Preethi Sheshadri (preethi.sheshadri@ukdri.ac.uk)

Acknowledgements

1028 The authors would like to thank the Michael J Fox Foundation and Parkinson's UK Foundation for generously
1029 funding our project. The authors would also like to express their gratitude to the members of the Michael Duchen
1030 and Gyorgy Szabadkai labs for their feedback, as well as to undergraduate students, including Shail Bhatt and
1031 Oriane Marguet, for their assistance with the preliminary data. We acknowledge the MRC Centre for
1032 Neuromuscular Diseases Biobank (supported by the National Institute for Health Research Biomedical Research
1033 Centres at Great Ormond Street Hospital for Children, NHS Foundation Trust) for providing the age- and sex-
1034 matched healthy controls and GBA1-E326K fibroblasts used in this study. Figure 6 was created using
1035 Biorender.com. We thank Dr. Elizabeth Slavik-Smith from the Electron Microscopy facility at UCL, Division of
1036 Biosciences, for her assistance with EM. We are also grateful for the help provided by Dr. Christopher Von
1037 Ruhland, Facility Lead (Electron and Light Microscopy), Central Biotechnology Services, Cardiff University,
1038 with the identification of the autophagic vesicles. The authors thank Professor Peter Holmans, Division of
1039 Psychological Medicine and Clinical Neurosciences, Cardiff University, for his help and guidance with the
1040 statistical analysis.

1041 **Table 1 – List of cell lines used**

Cell Lines used	Cell Line ID	Age/Sex	Cell type	Mutation	Source	Ethics Committee Approval
CONTROL 1	CONTROL 1	77/Male	Fibroblasts	No Mutation	NHNN	PD Royal Free Ethics
N370S	ND34263	65/Male	Fibroblasts; source for NH50182 iPSCs	GBA1-N370S; Heterozygous	NIH-RUCDR	
CONTROL 2	CONTROL 2	55/Male	Fibroblasts; source for Control1 iPSCs	No Mutation	NHNN	PD Royal Free Ethics
E326K 1	Het1/ JS48753	58/Male	Fibroblasts; source for Het1/E326K 1 iPSCs	GBA1-E326K; Heterozygous	NHNN	PD Royal Free Ethics
E326K 2	ND41015	63/Male	Fibroblasts; source for ND50045 iPSCs	GBA1-E326K; Heterozygous	NIH-RUCDR	
Isogenic Control (IsoC)	NH50142	63/Male	iPSCs; Isogenic Control for ND50045	CRISPR corrected GBA1-E326K heterozygous mutation	NIH-RUCDR	
E326K	ND50045	63/Male	iPSCs	GBA1-E326K; Heterozygous	NIH-RUCDR	
Isogenic Control (IsoC)	NH50186	65/Male	iPSCs; Isogenic Control for NH50182	CRISPR corrected GBA1-N370S heterozygous mutation	NIH-RUCDR	
N370S	NH50182	65/Male	iPSCs	GBA1-N370S; Heterozygous	NIH-RUCDR	
Control	Control 1	55/Male	iPSCs	No Mutation	Derived from CONTROL 2 fibroblasts	PD Royal Free Ethics for CONTROL 2 fibroblasts
E326K 1	Het1/ JS48753	58/Male	iPSCs	GBA1-E326K; Heterozygous	Derived from Het1 fibroblasts	PD Royal Free Ethics for JS48753 fibroblasts
E326K 2	Het 2/ MB240649	63/Male	iPSCs	GBA1-E326K; Heterozygous	Derived from MB240649 fibroblasts	PD Royal Free Ethics (for MB240649 fibroblasts
Control	SFC156 (Control 2)	65/Male	iPSCs	No Mutation	EBiSC	
N370S 1	SFC834 (N370S1)	72/Male	iPSCs	GBA1-N370S; Heterozygous	EBiSC	
N370S 2	SFC848 (N370S2)	68/Male	iPSCs	GBA1-N370S; Heterozygous	EBiSC	

1042 **Table 2 : List of antibodies used in the study**

Name	Catalogue no.	Host	Company	Application	Concentration
ATP6V0D2	AB194557	Mouse	Abcam	Western Blotting	1:1000
LAMP1 (H4A3)	sc-20011	Mouse	Santa Cruz	Western Blotting, Immunofluorescence	1:500
GBA (c-term)	64171	Rabbit	Sigma	Western Blotting	1:700
ATP6V1H	AB187706	Rabbit	Abcam	Western Blotting	1:1000
ATP6V1A	199326	Rabbit	Abcam	Western Blotting	1:1000
pMTOR	55365	Rabbit	Abcam	Western Blotting	1:1000
MTOR	45175	Mouse	Cell Signalling	Western Blotting	1:1000
ATG5 (D5F5U)	12994T	Rabbit	Cell Signalling	Western Blotting	1:1000
P62	610833	Mouse	BD Biosystems	Western Blotting	1:1000
LC3	L7543	Rabbit	Sigma	Western Blotting	1:1000
B-ACTIN	ab8226	Mouse	Cell Signalling	Western Blotting	1:5000
TOM20	ab186735	Rabbit	Abcam	Western Blotting	1:1000
LC3	PM036	Rabbit	MBL Biosystems	Immunofluorescence	1:500
Citrate Synthetase	ab96600	Rabbit	Abcam	Immunofluorescence	1:200
OXPHOS Cocktail	45-8199	Mouse	Thermoscientific	Western Blotting	1:1000
Alexa Fluor 488	A-11008	Goat	Thermoscientific	Immunofluorescence	1:1000
Alexa Fluor 594	A-11012	Goat	Thermoscientific	Immunofluorescence	1:1000
Alexa Fluor 647	A-21235	Goat	Thermoscientific	Immunofluorescence	1:1000
IRDye® 680RD Goat anti-Mouse	926-68070	Goat	Li-COR Biosciences	Western Blotting	1:10000
IRDye® 800CW Goat anti-Rabbit IgG	926-32211	Goat	Li-COR Biosciences	Western Blotting	1:10000

1043

Figure 1

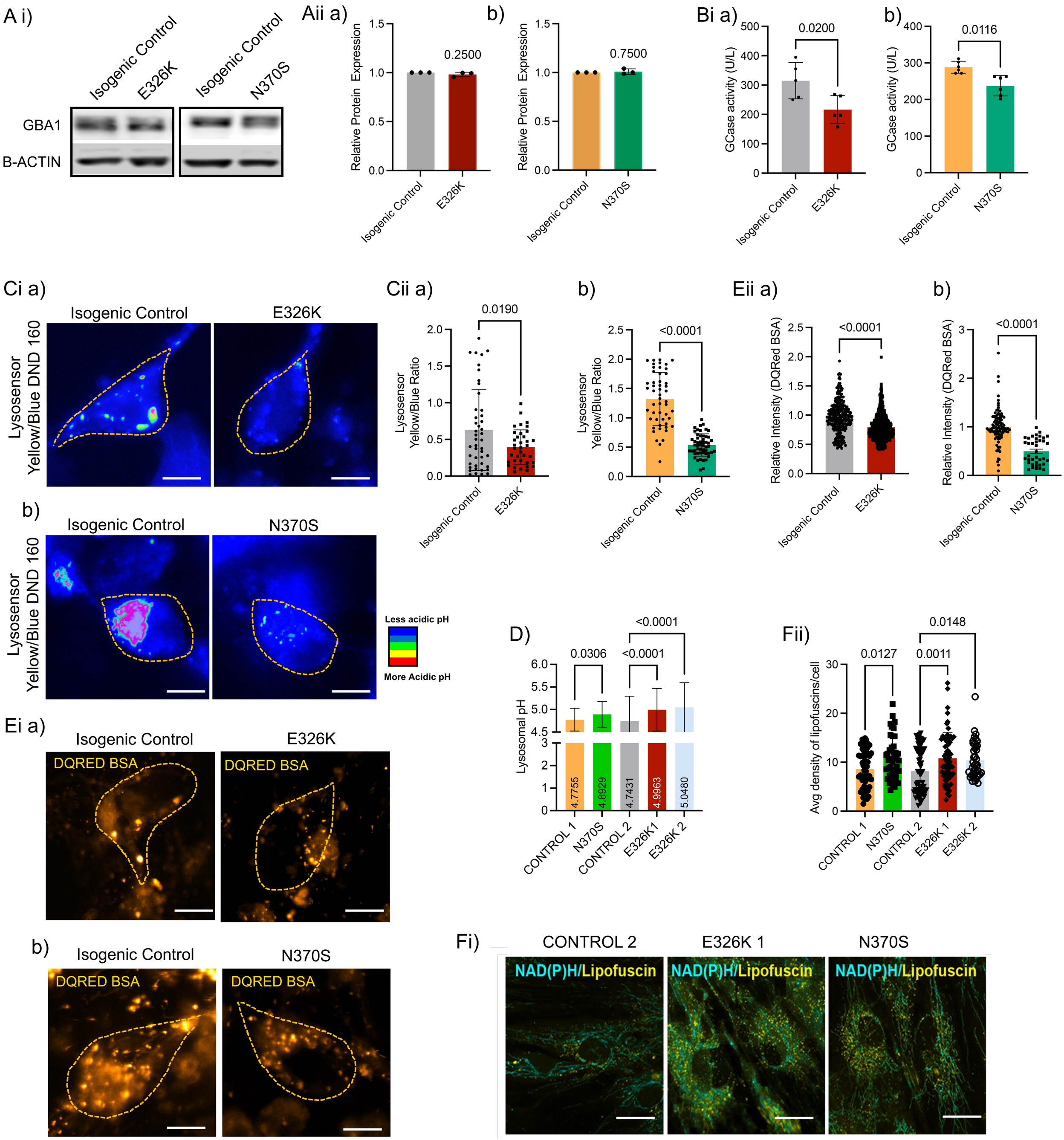
A i)
Isogenic Control
E326K
Isogenic Control
N370S
GBA1
B-ACTIN
Aii a)
b)
Relative Protein Expression
0.2500
0.7500
Isogenic Control
E326K
N370S
Bi a)
b)
GCase activity (U/L)
0.0200
0.0116
Ci a)
Isogenic Control
E326K
b)
Isogenic Control
N370S
Lysosensor Yellow/Blue DND 160
Less acidic pH
More Acidic pH
Cii a)
b)
Lysosensor Yellow/Blue Ratio
0.0190
<0.0001
Eii a)
b)
Relative Intensity (DQRed BSA)
<0.0001
Ei a)
Isogenic Control
E326K
b)
Isogenic Control
N370S
DQRED BSA
D)
Lysosomal pH
0.0306
<0.0001
<0.0001
4.7755
4.8929
4.7431
4.9963
5.0480
CONTROL 1
N370S
CONTROL 2
E326K1
E326K 2
Fii)
Avg density of lipofuscins/cell
0.0127
0.0011
0.0148
CONTROL 1
N370S
CONTROL 2
E326K 1
E326K 2
Fi)
CONTROL 2
E326K 1
N370S
NAD(P)H/Lipofuscin

Figure 2

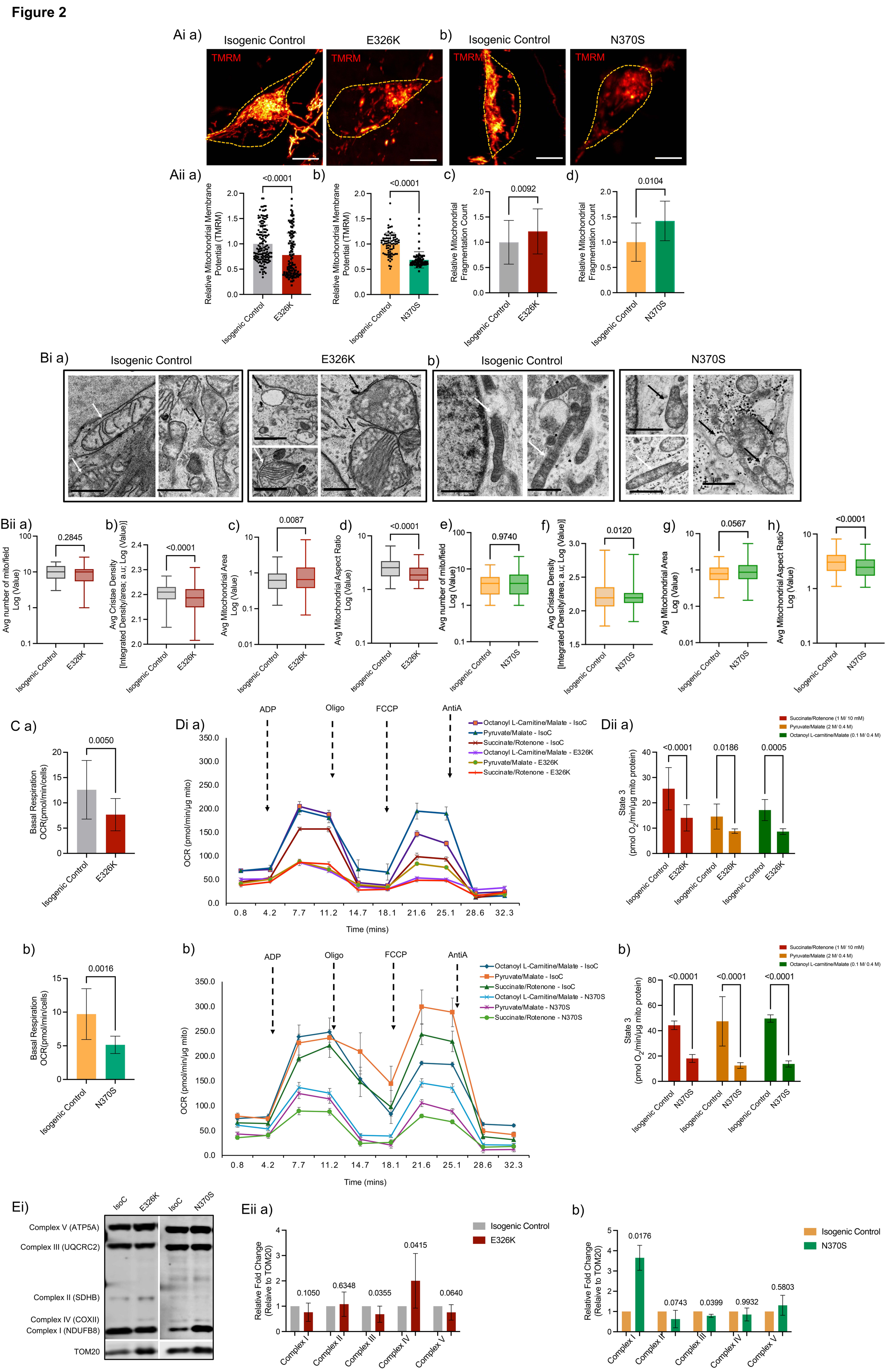
Ai a)
Isogenic Control
E326K
b)
Isogenic Control
N370S
TMRM
Aii a)
<0.0001
Relative Mitochondrial Membrane Potential (TMRM)
Isogenic Control
E326K
b)
<0.0001
Relative Mitochondrial Membrane Potential (TMRM)
Isogenic Control
N370S
c)
0.0092
Relative Mitochondrial Fragmentation Count
Isogenic Control
E326K
d)
0.0104
Relative Mitochondrial Fragmentation Count
Isogenic Control
N370S
Bi a)
Isogenic Control
E326K
b)
Isogenic Control
N370S
Bii a)
0.2845
Avg number of mito/field Log (Value)
b)
<0.0001
Avg Cristae Density [Integrated Density/area; a.u; Log (Value)]
c)
0.0087
Avg Mitochondrial Area Log (Value)
d)
<0.0001
Avg Mitochondrial Aspect Ratio Log (Value)
e)
0.9740
Avg number of mito/field Log (Value)
f)
0.0120
Avg Cristae Density [Integrated Density/area; a.u; Log (Value)]
g)
0.0567
Avg Mitochondrial Area Log (Value)
h)
<0.0001
Avg Mitochondrial Aspect Ratio Log (Value)
Isogenic Control
E326K
N370S
C a)
0.0050
Basal Respiration OCR(pmol/min/cells)
Isogenic Control
E326K
Di a)
ADP
Oligo
FCCP
AntiA
Octanoyl L-Carnitine/Malate - IsoC
Pyruvate/Malate - IsoC
Succinate/Rotenone - IsoC
Octanoyl L-Carnitine/Malate - E326K
Pyruvate/Malate - E326K
Succinate/Rotenone - E326K
OCR (pmol/min/µg mito)
Time (mins)
Dii a)
Succinate/Rotenone (1 M/ 10 mM)
Pyruvate/Malate (2 M/ 0.4 M)
Octanoyl L-carnitine/Malate (0.1 M/ 0.4 M)
<0.0001
0.0186
0.0005
State 3 (pmol O2/min/µg mito protein)
Isogenic Control
E326K
b)
0.0016
Basal Respiration OCR(pmol/min/cells)
Isogenic Control
N370S
b)
ADP
Oligo
FCCP
AntiA
Octanoyl L-Carnitine/Malate - IsoC
Pyruvate/Malate - IsoC
Succinate/Rotenone - IsoC
Octanoyl L-Carnitine/Malate - N370S
Pyruvate/Malate - N370S
Succinate/Rotenone - N370S
OCR (pmol/min/µg mito)
Time (mins)
b)
Succinate/Rotenone (1 M/ 10 mM)
Pyruvate/Malate (2 M/ 0.4 M)
Octanoyl L-carnitine/Malate (0.1 M/ 0.4 M)
<0.0001
<0.0001
<0.0001
State 3 (pmol O2/min/µg mito protein)
Isogenic Control
N370S
Ei)
IsoC
E326K
IsoC
N370S
Complex V (ATP5A)
Complex III (UQCRC2)
Complex II (SDHB)
Complex IV (COXII)
Complex I (NDUFB8)
TOM20
Eii a)
Isogenic Control
E326K
0.1050
0.6348
0.0355
0.0415
0.0640
Relative Fold Change (Relative to TOM20)
Complex I
Complex II
Complex III
Complex IV
Complex V
b)
Isogenic Control
N370S
0.0176
0.0743
0.0399
0.9932
0.5803
Relative Fold Change (Relative to TOM20)
Complex I
Complex II
Complex III
Complex IV
Complex V

Figure 3

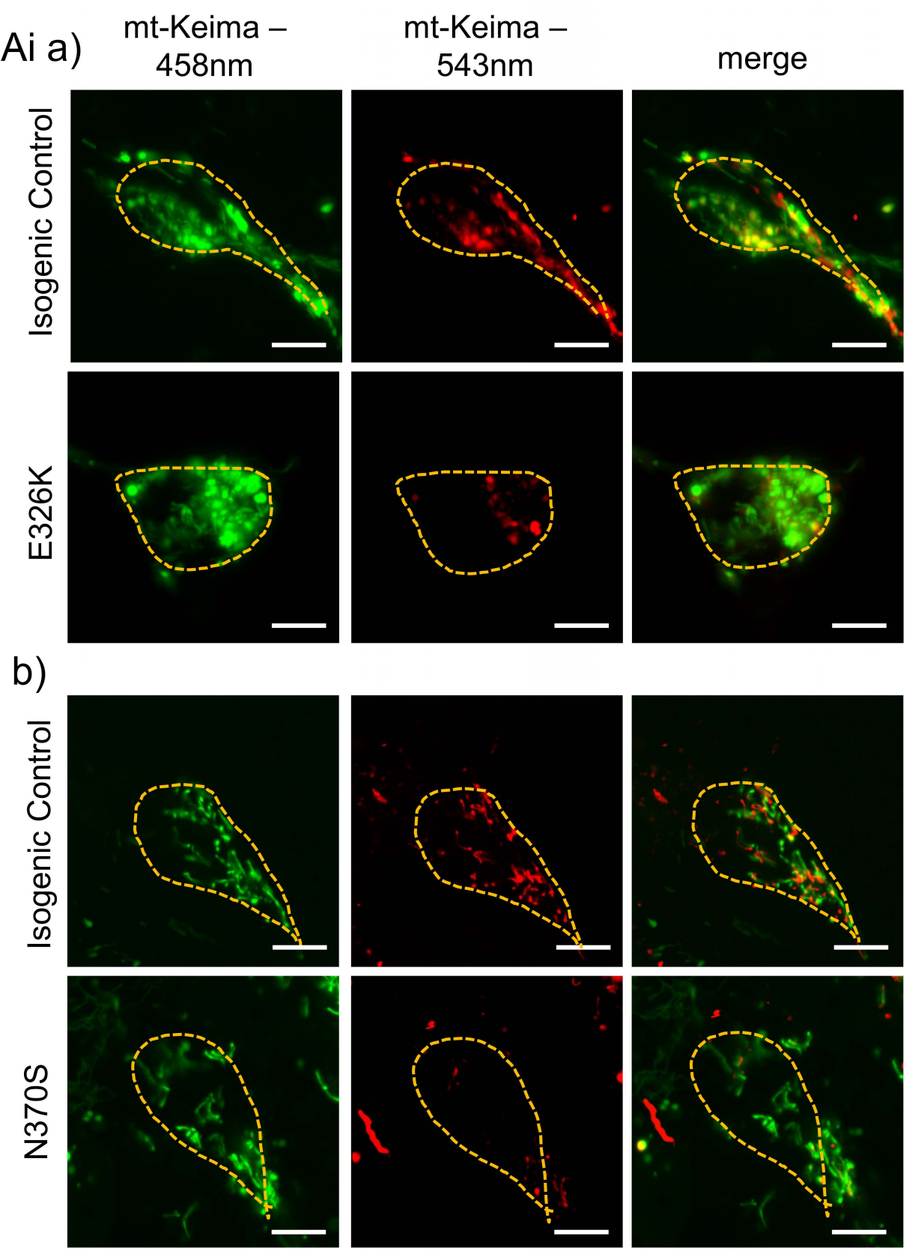
Ai a)
mt-Keima – 458nm
mt-Keima – 543nm
merge
Isogenic Control
E326K
b)
Isogenic Control
N370S

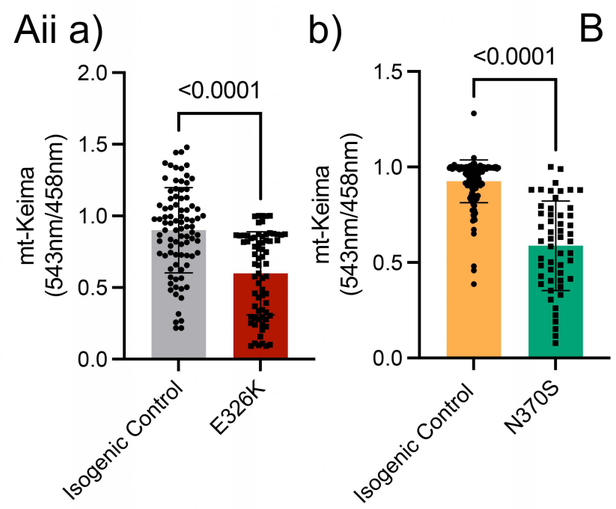
Aii a)
b)
mt-Keima (543nm/458nm)
<0.0001
Isogenic Control
E326K
N370S

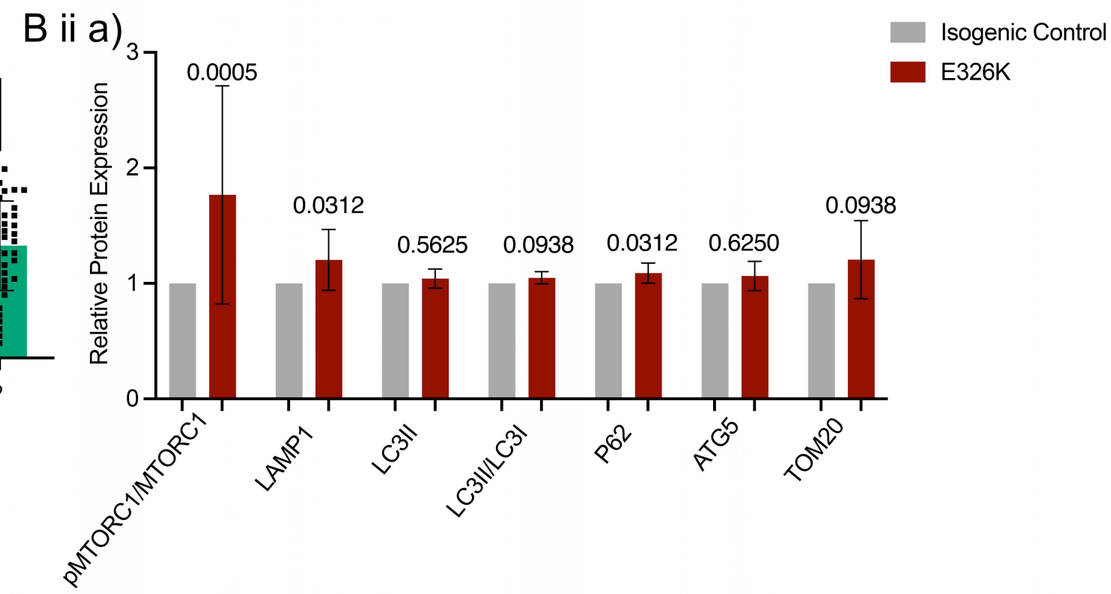
B ii a)
Isogenic Control
E326K
Relative Protein Expression
0.0005
0.0312
0.5625
0.0938
0.0312
0.6250
0.0938
pMTORC1/MTORC1
LAMP1
LC3II
LC3II/LC3I
P62
ATG5
TOM20

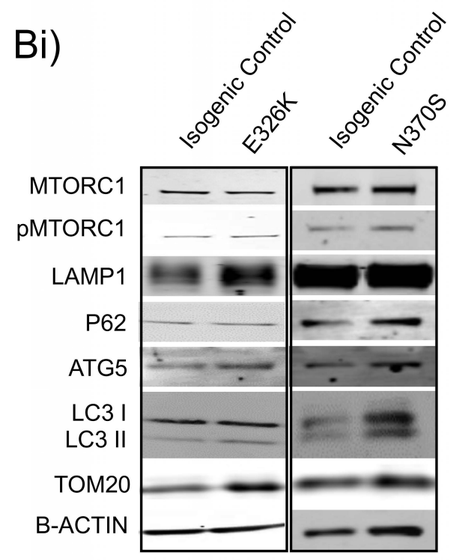
Bi)
Isogenic Control
E326K
Isogenic Control
N370S
MTORC1
pMTORC1
LAMP1
P62
ATG5
LC3 I
LC3 II
TOM20
B-ACTIN

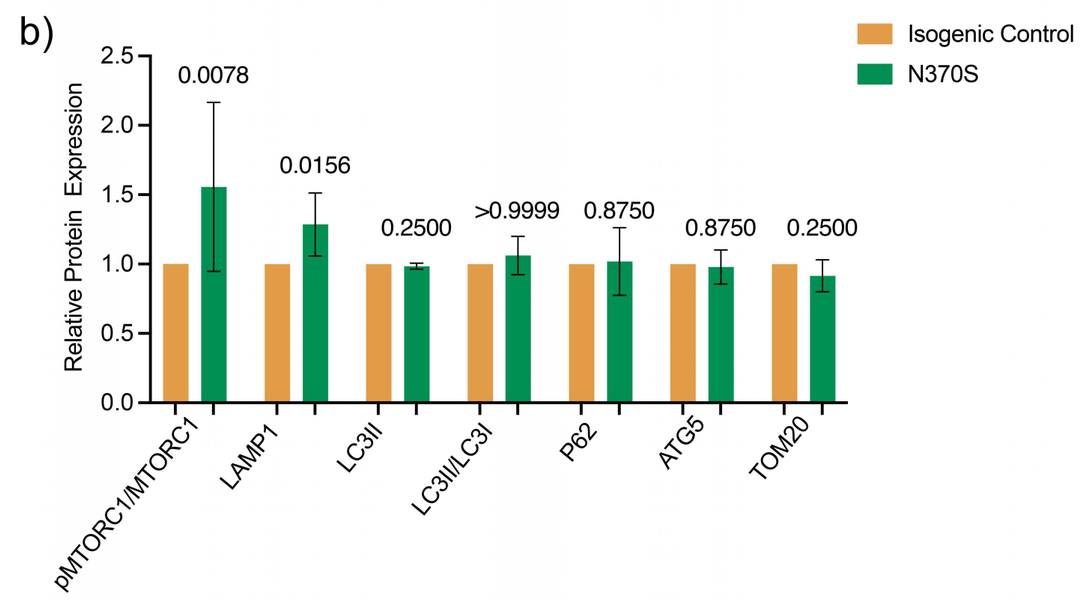
b)
Isogenic Control
N370S
Relative Protein Expression
0.0078
0.0156
0.2500
>0.9999
0.8750
0.8750
0.2500
pMTORC1/MTORC1
LAMP1
LC3II
LC3II/LC3I
P62
ATG5
TOM20

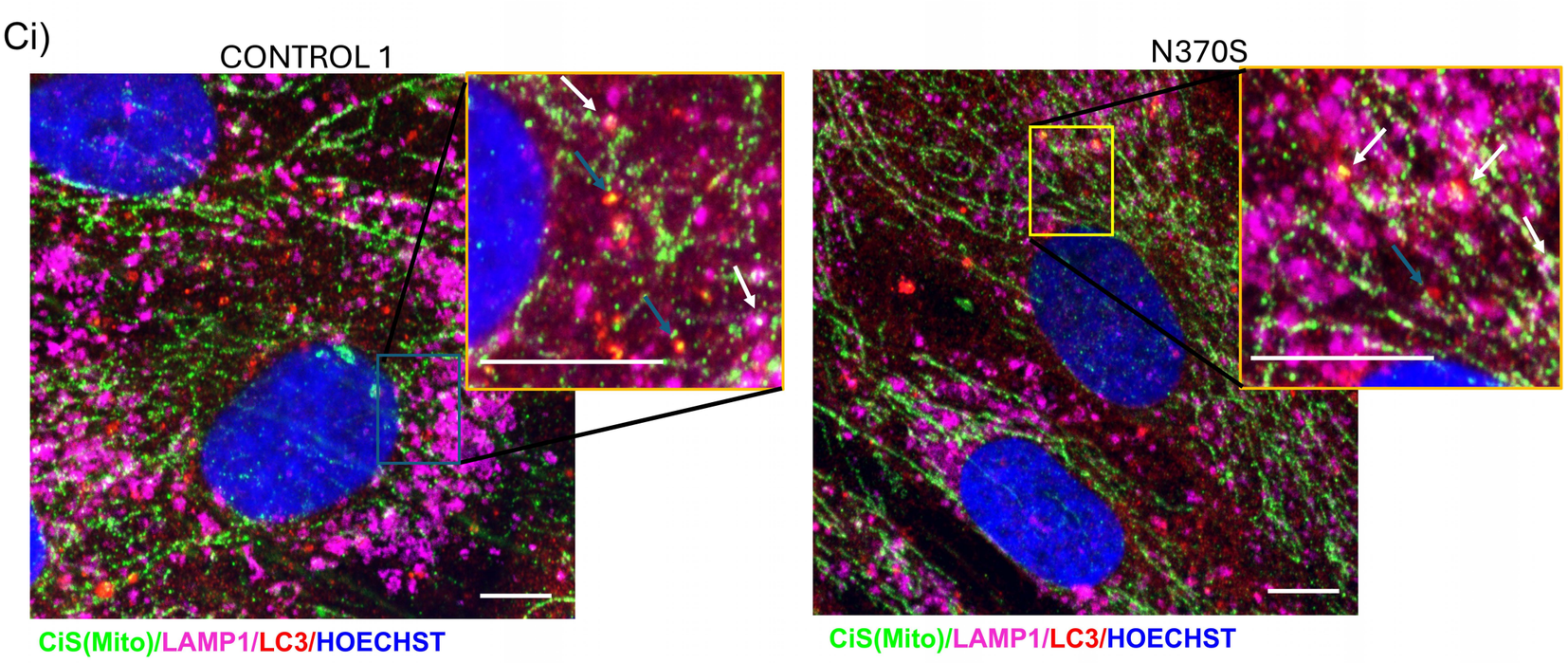
Ci)
CONTROL 1
N370S
CiS(Mito)/LAMP1/LC3/HOECHST
CiS(Mito)/LAMP1/LC3/HOECHST

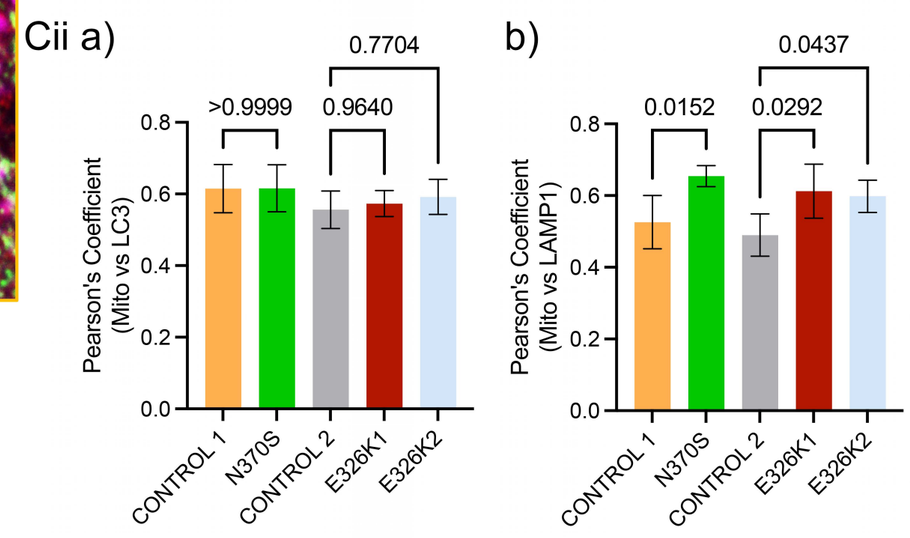
Cii a)
b)
Pearson's Coefficient (Mito vs LC3)
Pearson's Coefficient (Mito vs LAMP1)
>0.9999
0.9640
0.7704
0.0152
0.0292
0.0437
CONTROL 1
N370S
CONTROL 2
E326K1
E326K2

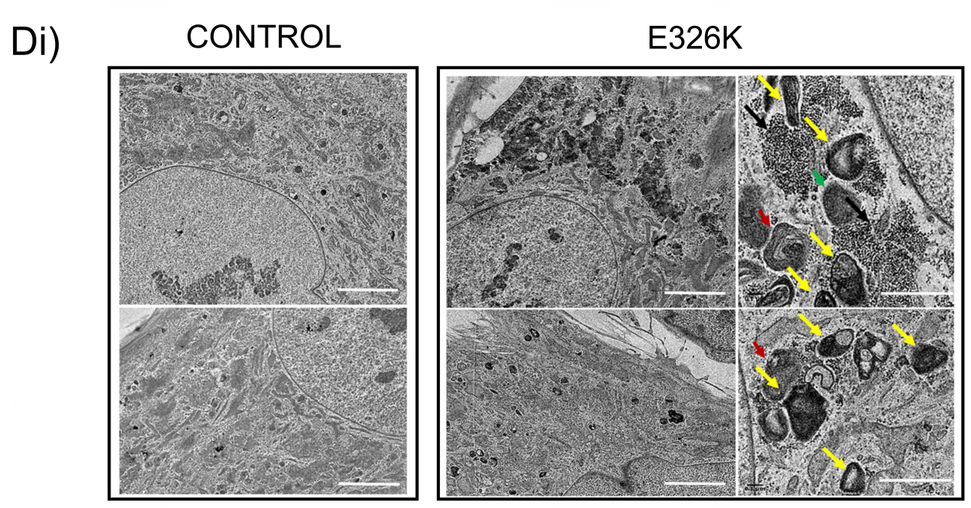
Di)
CONTROL
E326K

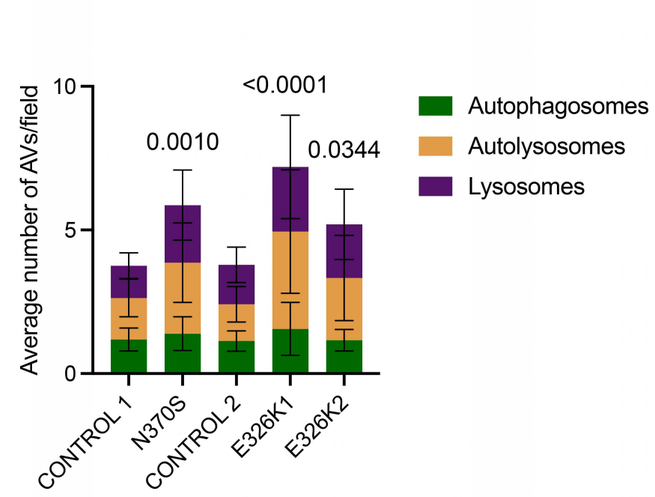
D ii)
Average number of AVs/field
0.0010
<0.0001
0.0344
Autophagosomes
Autolysosomes
Lysosomes
CONTROL 1
N370S
CONTROL 2
E326K1
E326K2

Figure 4

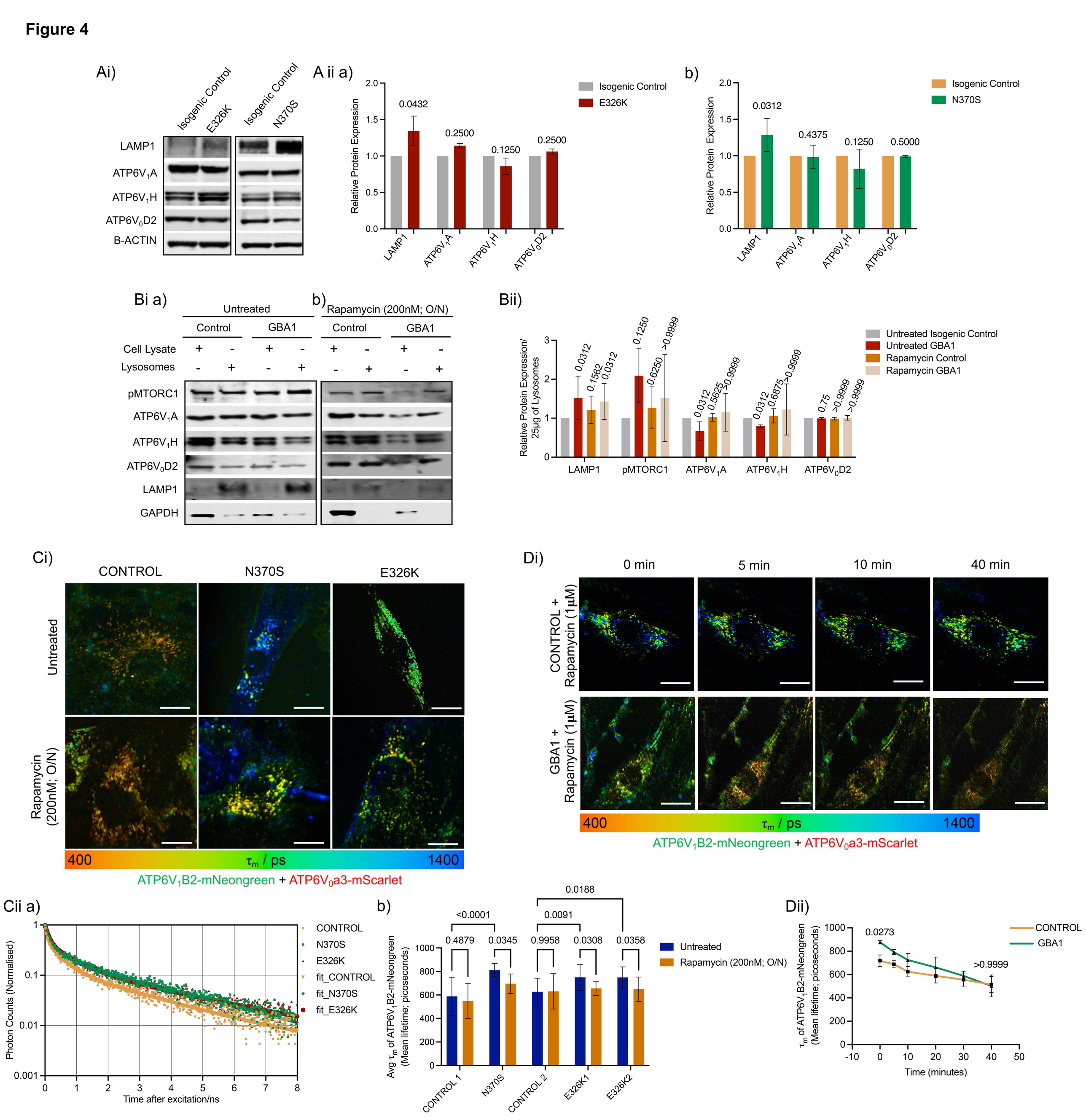
Ai)
Isogenic Control
E326K
Isogenic Control
N370S
LAMP1
ATP6V1A
ATP6V1H
ATP6V0D2
B-ACTIN
A ii a)
Isogenic Control
E326K
Relative Protein Expression
0.0432
0.2500
0.1250
0.2500
LAMP1
ATP6V1A
ATP6V1H
ATP6V0D2
b)
Isogenic Control
N370S
0.0312
0.4375
0.1250
0.5000
Bi a)
Untreated
Control
GBA1
Cell Lysate
Lysosomes
pMTORC1
ATP6V1A
ATP6V1H
ATP6V0D2
LAMP1
GAPDH
b)
Rapamycin (200nM; O/N)
Bii)
Untreated Isogenic Control
Untreated GBA1
Rapamycin Control
Rapamycin GBA1
Relative Protein Expression/ 25µg of Lysosomes
0.0312
0.1562
0.0312
0.1250
0.6250
>0.9999
0.0312
0.5625
>0.9999
0.0312
0.6875
>0.9999
0.75
>0.9999
>0.9999
Ci)
CONTROL
N370S
E326K
Untreated
Rapamycin (200nM; O/N)
400
τm / ps
1400
ATP6V1B2-mNeongreen + ATP6V0a3-mScarlet
Di)
0 min
5 min
10 min
40 min
CONTROL + Rapamycin (1µM)
GBA1 + Rapamycin (1µM)
400
τm / ps
1400
ATP6V1B2-mNeongreen + ATP6V0a3-mScarlet
Cii a)
Photon Counts (Normalised)
Time after excitation/ns
CONTROL
N370S
E326K
fit_CONTROL
fit_N370S
fit_E326K
b)
Avg τm of ATP6V1B2-mNeongreen (Mean lifetime; picoseconds)
0.0188
<0.0001
0.0091
0.4879
0.0345
0.9958
0.0308
0.0358
Untreated
Rapamycin (200nM; O/N)
CONTROL 1
N370S
CONTROL 2
E326K1
E326K2
Dii)
τm of ATP6V1B2-mNeongreen (Mean lifetime; picoseconds)
0.0273
>0.9999
CONTROL
GBA1
Time (minutes)

Figure 5

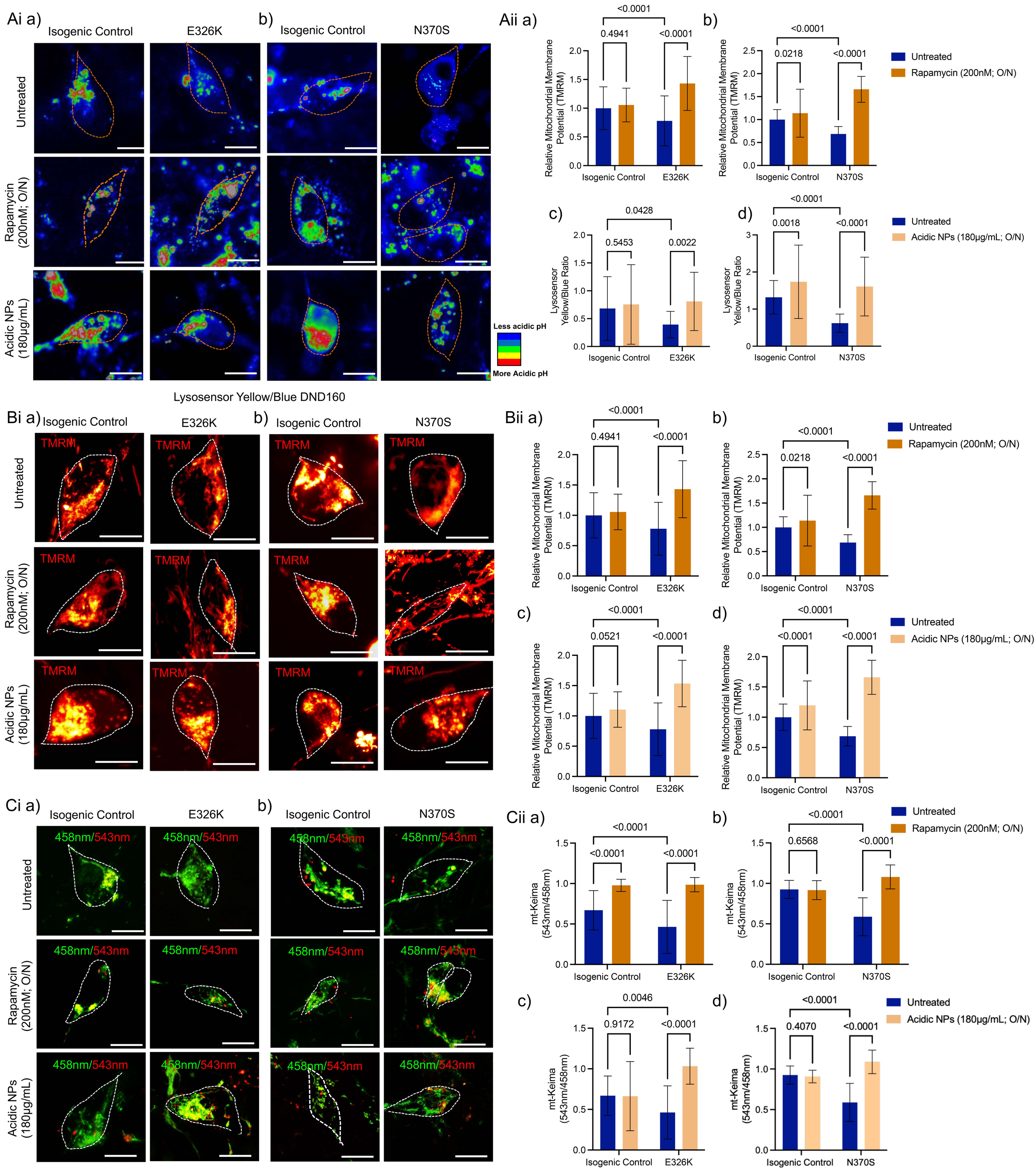
Ai a)
Isogenic Control
E326K
b)
Isogenic Control
N370S
Untreated
Rapamycin (200nM; O/N)
Acidic NPs (180µg/mL)
Less acidic pH
More Acidic pH
Lysosensor Yellow/Blue DND160
Aii a)
b)
c)
d)
Relative Mitochondrial Membrane Potential (TMRM)
Lysosensor Yellow/Blue Ratio
Untreated
Rapamycin (200nM; O/N)
Acidic NPs (180µg/mL; O/N)
Bi a)
b)
TMRM
Bii a)
b)
c)
d)
Ci a)
b)
458nm/543nm
Cii a)
b)
c)
d)
mt-Keima (543nm/458nm)

Figure 6

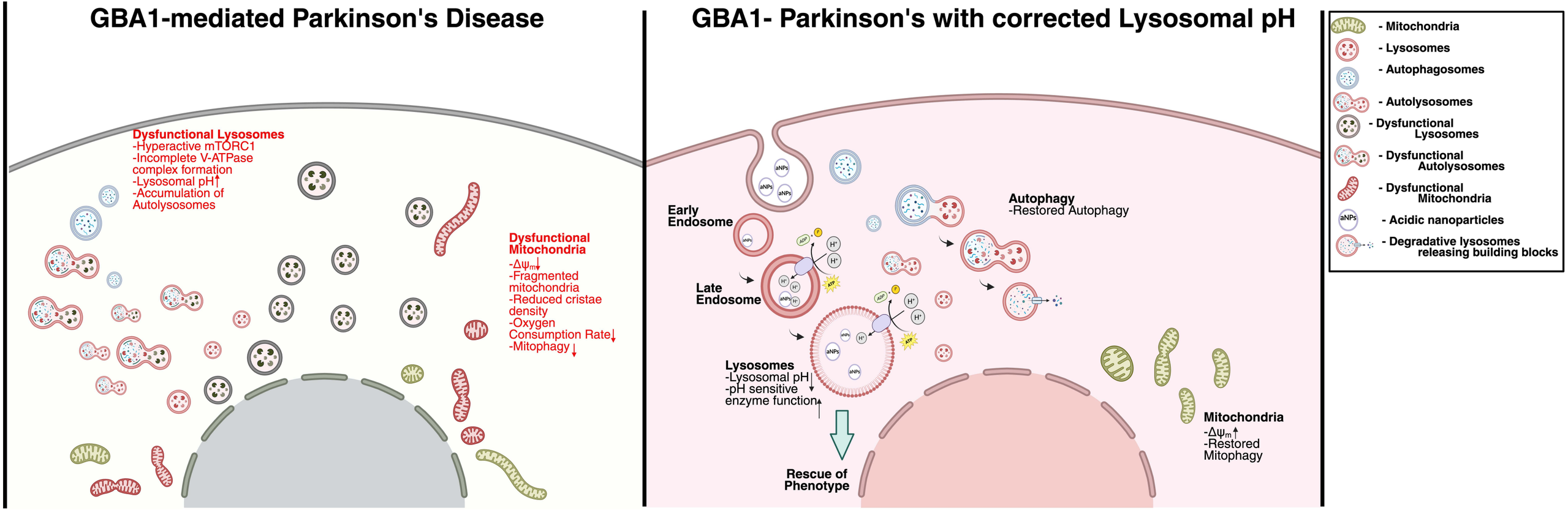
GBA1-mediated Parkinson's Disease
Dysfunctional Lysosomes
-Hyperactive mTORC1
-Incomplete V-ATPase complex formation
-Lysosomal pH↑
-Accumulation of Autolysosomes
Dysfunctional Mitochondria
-Δψm↓
-Fragmented mitochondria
-Reduced cristae density
-Oxygen Consumption Rate↓
-Mitophagy↓
GBA1- Parkinson's with corrected Lysosomal pH
Early Endosome
Late Endosome
Lysosomes
-Lysosomal pH↓
-pH sensitive enzyme function↑
Rescue of Phenotype
Autophagy
-Restored Autophagy
Mitochondria
-Δψm↑
-Restored Mitophagy
aNPs
ADP
ATP
H+
- Mitochondria
- Lysosomes
- Autophagosomes
- Autolysosomes
- Dysfunctional Lysosomes
- Dysfunctional Autolysosomes
- Dysfunctional Mitochondria
- Acidic nanoparticles
- Degradative lysosomes releasing building blocks

Supplementary Figure 1

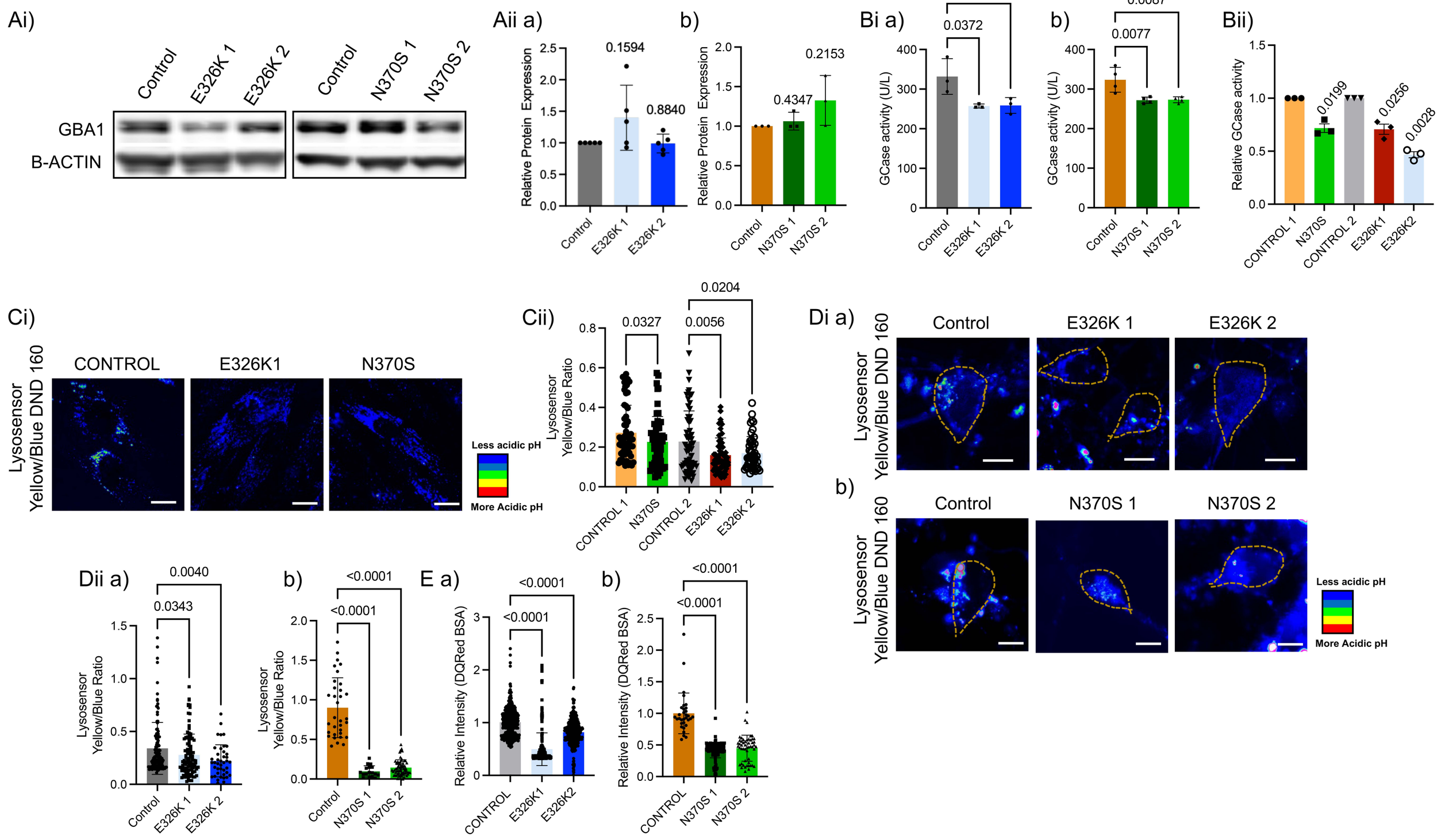

Supplementary Figure 2

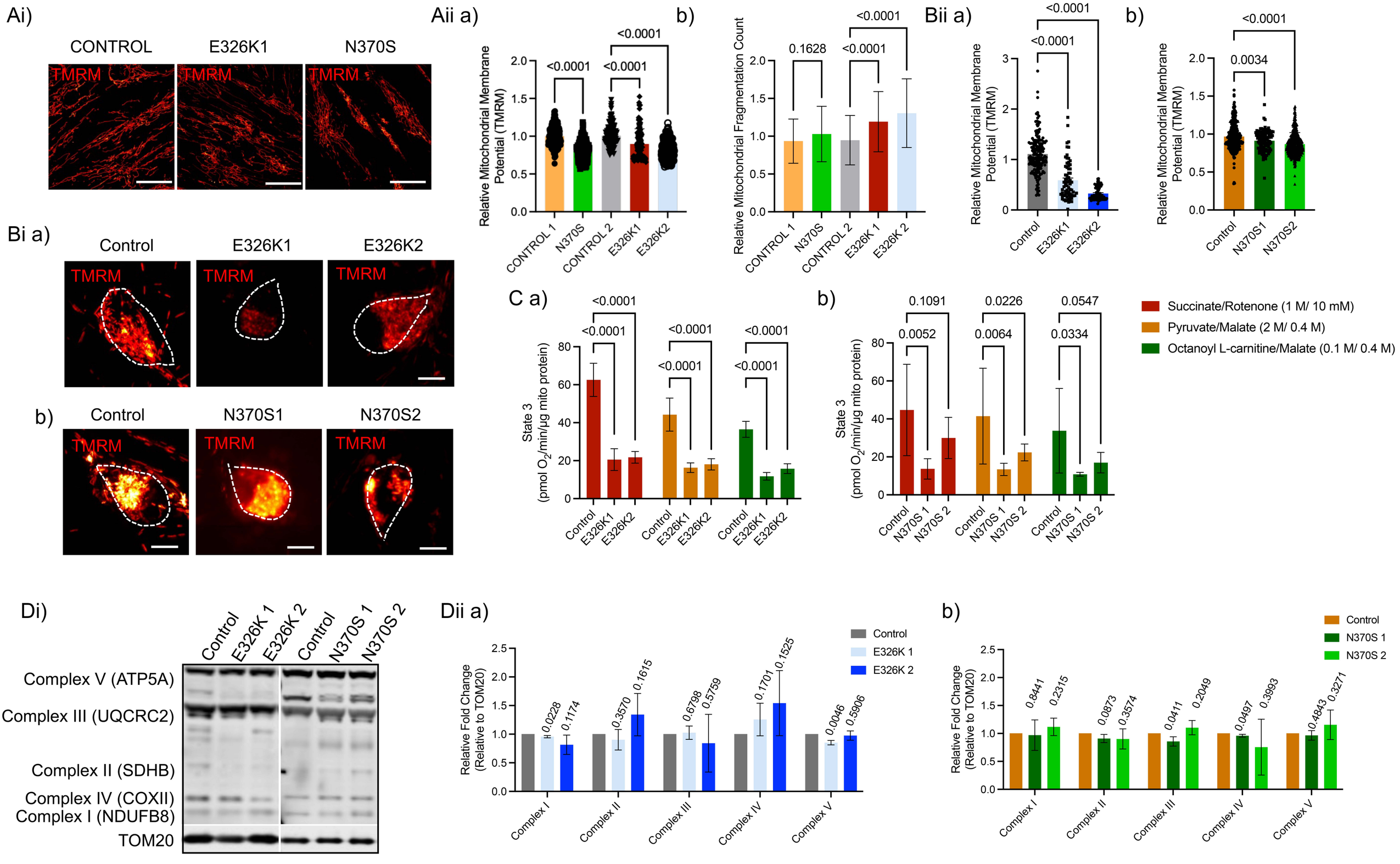

Supplementary Figure 3

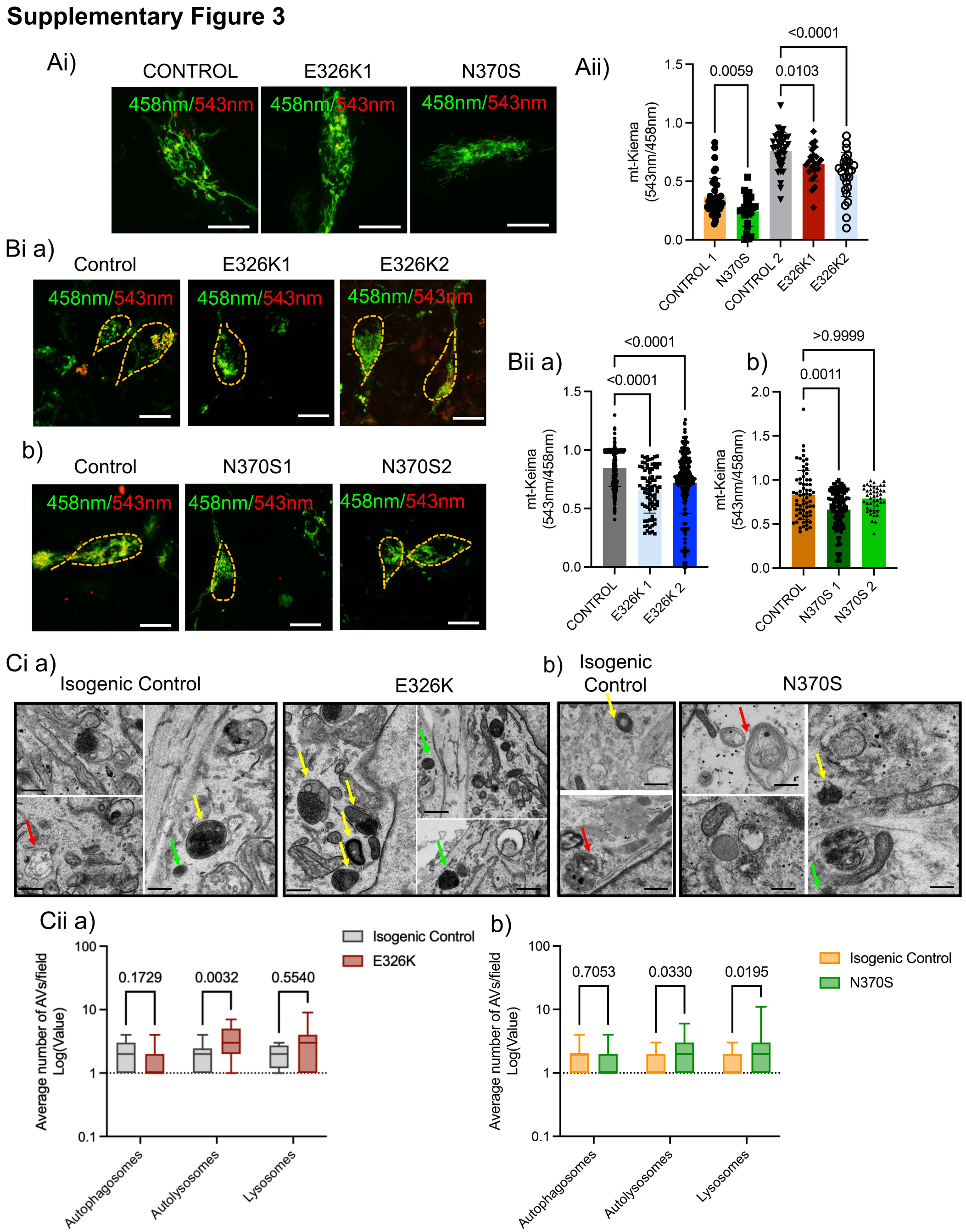
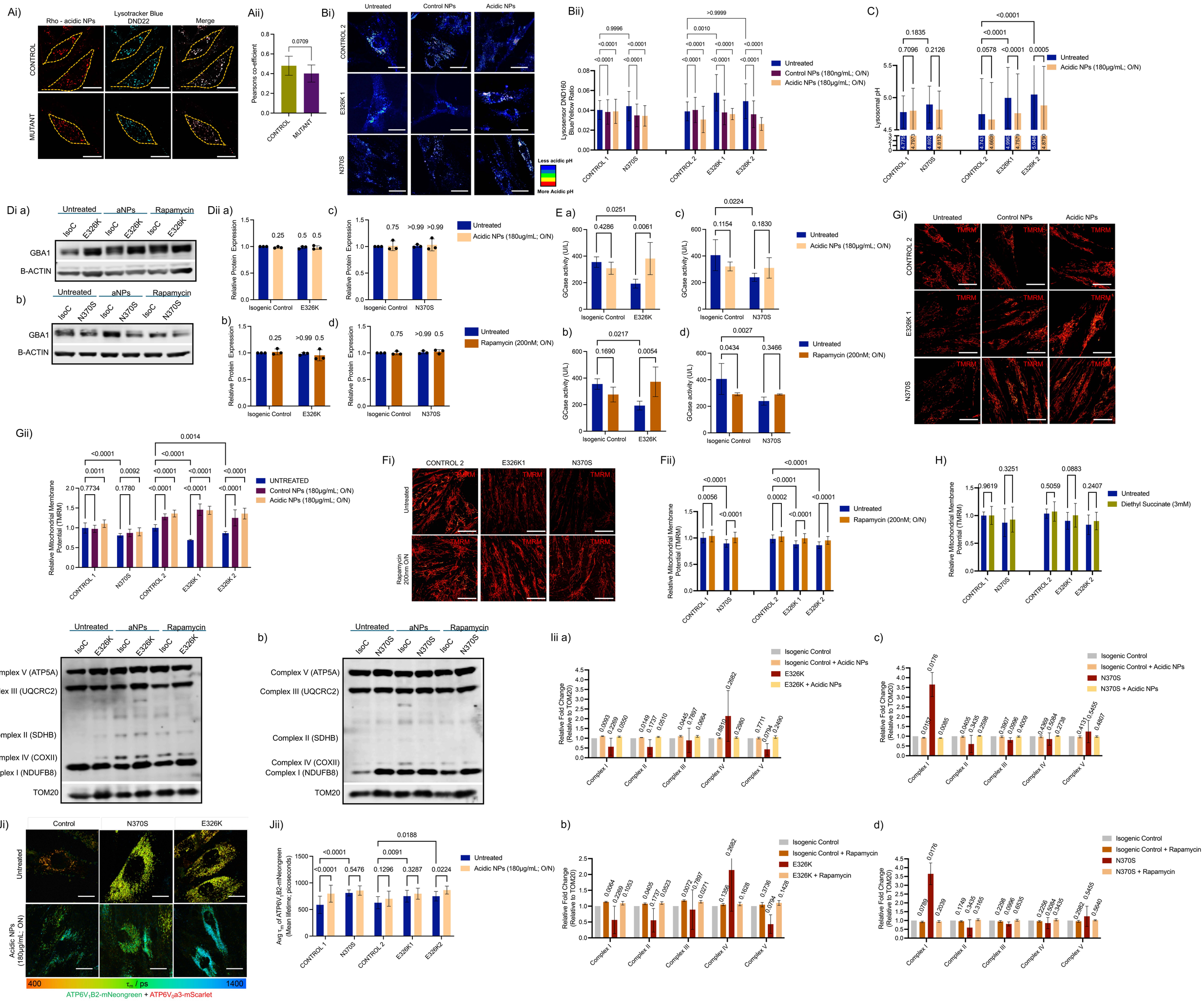
Supplementary Figure 4